



TUM School of Natural Sciences

Technische Universität München

Nuclear Structure Investigations of Light Nuclei  
with the R3B Experiment

Tobias Jenegger

Vollständiger Abdruck der von der TUM School of Natural Sciences der Technischen  
Universität München zur Erlangung des akademischen Grades eines  
Doktors der Naturwissenschaften (Dr. rer. nat.)  
genehmigten Dissertation.

Vorsitz:

Apl. Prof. Dr. Norbert Kaiser

Prüfer\*innen der Dissertation:

1. Prof. Dr. Laura Fabbietti

2. Prof. Dr. Lothar Oberauer

Die Dissertation wurde am DATUM-HIER bei der Technischen Universität München  
eingereicht und durch die TUM School of Natural Sciences am DATUM-HIER  
angenommen.





TUM School of Natural Sciences

---

Nuclear Structure Investigations of Light Nuclei  
with the R3B Experiment

---

Tobias Jenegger



Techinsche Universität München  
Fachbereich: Dense and Strange Hadronic Matter (E62)

2023



# Abstract

Astrophysical observations of neutron stars (NS) provide rather precise data about the global properties of such unique and fascinating objects, e.g., the mass and radius. For the interpretation of this data and to gain a profound understanding of the inner structure of NS, it is essential to investigate nuclear matter under extreme conditions. A key instrument to describe nuclear matter over a wide density range is the equation of state (EOS). The radius and stability of NS are governed by the pressure of the highly asymmetric matter in the inside, which is defined by the so-called symmetry energy in the EOS. This quantity and especially its slope parameter L around nuclear saturation density are experimentally only weakly constraint so far.

A experimental attempt to constrain the L parameter is to measure the neutron-skin thickness of highly asymmetric nuclei since both quantities are directly correlated. One of the most established experimental methods to probe the nuclear density distribution is the measurement of total interaction cross section at radioactive beam facilities. A common method to describe integrated cross sections is the Glauber reaction model. In such a model, which includes realistic in-medium modification for composite nuclei, the only inputs are the experimental nucleon-nucleon cross sections and the density distribution of the projectile and target nucleus.

For a precise determination of the neutron-skin thickness of exotic nuclei, and thus to constrain the symmetry energy slope parameter, it is essential to quantify the uncertainty of the reaction model under ideal conditions.

This work provides a detailed summary of the precise measurement of total interaction cross sections of  $^{12}\text{C} + ^{12}\text{C}$  collisions in the energy regime between 400 and 1000 MeV/nucleon. The underlying experiment was carried out as part of the commissioning of the R<sup>3</sup>B setup during the FAIR Phase-0 campaign at GSI. The present analysis of total interaction cross sections is based on a transmission measurement, where the numbers of incoming and non-reacted projectiles before and after the reaction target have been identified. The identification of the non-reacted  $^{12}\text{C}$  poses a challenge to the experimental setup since the time- and rate-dependent detector efficiency, as well as the geometrical acceptance of the whole setup, have to be considered.

The presented cross sections was determined with a total experimental uncertainty down to 0.4 % and represent the most precise data currently available in this energy regime. The validity of the measurement and analysis method was confirmed by data from previous experiments. It was shown that predictions based on a realistic Glauber reaction model are in good agreement with the presented experimental results for low energy but overestimate them by around 2.5 % at higher energies.





# Contents

<b>1</b>	<b>Introduction</b>	<b>1</b>
1.1	Nuclear Structure Models . . . . .	1
1.2	Astrophysical interest . . . . .	1
1.3	EOS and constraining parameter L . . . . .	1
<b>2</b>	<b>Reaction Models</b>	<b>1</b>
2.1	Glauber Theory . . . . .	1
2.2	Quasi-Free Scattering (QFS) Reactions . . . . .	1
2.2.1	Kinematics of QFS Reactions . . . . .	2
2.2.2	Cross Sections for QFS Reactions - Qualitative Considerations .	4
2.2.3	Application Fields of QFS Reactions . . . . .	4
<b>3</b>	<b>Experiment</b>	<b>4</b>
3.1	GSI facility . . . . .	5
3.1.1	FAIR Project . . . . .	5
3.2	R3B Setup . . . . .	6
3.3	Detector Setup in S444 Commissioning Experiment 2020 . . . . .	7
3.3.1	Multi Wire Proportional Chambers (MWPC) . . . . .	7
3.3.2	Ionisation Chambers - R3BMusic/TWIM Music . . . . .	8
3.3.3	Sofia Start Detector . . . . .	11
3.3.4	GLAD Magnet . . . . .	12
3.3.5	CALIFA Calorimeter . . . . .	12
3.3.6	Sofia Time of Flight Wall . . . . .	19
3.3.7	NeuLAND Detector . . . . .	20
3.3.8	Calibration of the Detector Systems . . . . .	20
<b>4</b>	<b>Analysis - Total Interaction Cross Section of <math>^{12}\text{C} + ^{12}\text{C}</math></b>	<b>21</b>
4.1	Cross Section Measurement via Transmission Method . . . . .	21
4.2	Event Selection . . . . .	23
4.3	Charge Changing Cross Section Measurement . . . . .	28
4.3.1	TWIN MUSIC Calibration . . . . .	28
4.3.2	TWIN MUSIC Event Selection . . . . .	29
4.3.3	Carbon Identification . . . . .	30
4.4	Geometric Corrections . . . . .	38
4.5	Isotope Correction - Total Interaction Cross Section . . . . .	41
4.5.1	Results for Isotope Correction Methods . . . . .	48

4.6	Statistical and Systematic Error Analysis . . . . .	51
4.6.1	Statistical Uncertainties . . . . .	52
4.6.2	Systematic Uncertainties . . . . .	52
4.7	(Preliminary) Results Total Interaction Cross Section . . . . .	52
4.8	Quasi-Free Scattering $^{12}\text{C}(\text{p},2\text{p})^{11}\text{B}$ . . . . .	52
4.9	reaction cross section Analysis . . . . .	54
<b>5</b>	<b>Results and Discussion</b>	<b>54</b>
	<b>Appendices</b>	<b>54</b>
<b>A</b>	<b>TWIN MUSIC Geometric Acceptance Correction via Efficiency Measurement</b>	<b>54</b>
<b>B</b>	<b>appendix-test</b>	<b>55</b>
<b>C</b>	<b>second stuff I want to add</b>	<b>56</b>
	<b>References</b>	<b>56</b>

# 1 Introduction

Talk something about first ideas from Greeks of the structure of matter /historical part  
 Comparisons between atomic model and nuclear models

## 1.1 Nuclear Structure Models

## 1.2 Astrophysical interest

NS and NS mergers & R-process & termination via fission

## 1.3 EOS and constraining parameter L

# 2 Reaction Models

## 2.1 Glauber Theory

## 2.2 Quasi-Free Scattering (QFS) Reactions

Quasi-free scattering (QFS) reactions, as a subset of direct reactions, are processes where a projectile nucleon interacts with a target nucleon in a single, fast, and highly localized event. The timescale of these interactions is extremely short, approximately  $10^{-21}$  s, implying that the relative kinetic energies of the participants are high, typically  $\gtrsim 100$  AMeV.

In QFS experiments conducted in direct kinematics, a proton serves as the projectile, colliding with a nucleon or a cluster within the target nucleus. Conversely, in inverse kinematics, the nucleus of interest becomes the projectile, while a proton or proton-like particle is used as the target. Despite these differing setups, both approaches are fundamentally equivalent, differing only due to a Lorentz transformation of the reference frame.

As the name implies, QFS reactions are conceptually similar to free nucleon-nucleon scattering, with the primary approximation being that the influence of the residual nucleus is neglected to first order. This approximation simplifies the theoretical description of the process, allowing to treat the interaction as a two-body problem within a (only weakly interfering) nuclear environment.

The first experiments confirming the existence of quasi-free scattering processes were conducted at the University of California, Berkeley, in 1952 by O. Chamberlain and Emilio Segrè[1]. In their study, lithium nuclei were bombarded with 350 MeV protons, and coincident proton pairs were observed with an opening angle of approximately 90°.

That same year, J.B. Cladis, W.N. Hess, and B.J. Moyer published results on the scattering of 340 MeV protons on deuterium and carbon targets[2], further substantiating the phenomenon.

In 1957, Tyren, Maris, and Hillman designed an experiment aimed at fully characterizing proton-proton collisions within the quasi-free scattering framework[3]. Their results validated the assumption of a direct and clean interaction between the projectile and the target nucleon, free from significant distortions caused by the surrounding nucleus. Furthermore, these experiments demonstrated that QFS reactions could serve as a powerful tool for probing nuclear structure and testing predictions of the shell model. Specifically, they enabled the study of key nuclear parameters such as spin-orbit splitting and energy differences between nuclear shells and hence to probe the shell evolution.

In QFS reactions, these parameters can be extracted by analyzing the reaction products, which include the two correlated outgoing protons, the residual nucleus, and any gamma rays emitted during de-excitation of the residual nucleus. The detailed measurements of these observables provide critical insights into the underlying nuclear structure and dynamics.

The experimental discoveries and theoretical insights from these early studies catalyzed significant advancements in the theoretical modeling of QFS reactions. These models have since become essential tools for understanding nucleon-nucleon interactions within the nuclear medium and for refining our knowledge of nuclear structure and reaction mechanisms.

### 2.2.1 Kinematics of QFS Reactions

A simplified picture, which however explains the essential physics of the QFS reaction, can be found in figure 1: we have an incoming proton knocking out a nuclear constituent (proton/neutron) in a free nucleon-nucleon collision ending with a final state having the scattered proton, the scattered off nuclear constituent and the rest nucleus ( $A-1$ )\*. In this picture index  $0$  is assigned to the incoming proton,  $1$  to the knocked out nucleon,  $2$  to the outgoing projectile proton,  $A$  to the initial nucleus and  $A-1$  to the final nucleus accordingly. From energy -momentum conservation the reaction can be expressed as:

$$P_A + P_0 = P_1 + P_2 + P_{A-1} \quad (1)$$

with  $P_i$  the four momentum ( $\mathbf{p}_i, E_i$ ).

In direct kinematics as presented in figure 1 the separation of the ejected nucleon for a

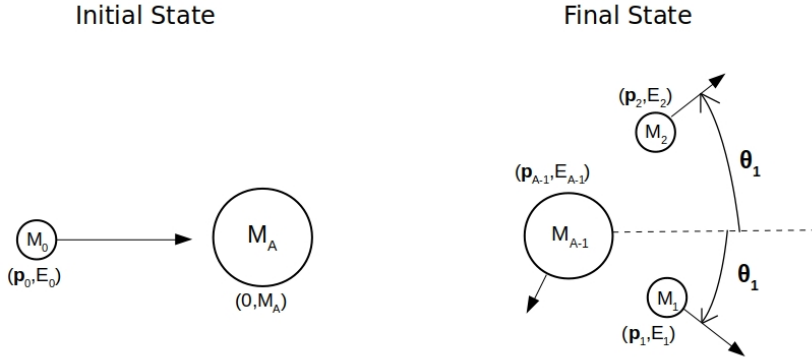


Figure 1: Simplified picture of the QFS reaction process in direkt kinematics.

certain final state of the nucleus  $A-1$  is given by<sup>1</sup>:

$$S = T_0 - (T_1 + T_2 + T_{A-1}); \text{ with } T_i \text{ the kinetic energy of particle } i \quad (2)$$

In the idealized shell model the separation energy equals to the (negative) energy of the nucleus' single-particle state. For the case the proton knocks out the least bound nucleon (proton/neutron) the final nucleus is lying in the ground state with  $E_{A-1} = M_{A-1}c^2 + T_{A-1}$ .

If a nucleon has been ejected from an inner shell resulting in a hole state, the final nucleus will be in an excited state:

$$E_{A-1}^* = M_{A-1}c^2 + T_{A-1} + E_{exe} \quad (3)$$

The excitation energy  $E_{exe}$  is reflected in the difference in the separation energy of the least bound nucleon and the ejected one. From the experimental point of view  $E_{exe}$  is directly accessible via gamma detection from the transition of the final nucleus from the excited to the ground state. According to the picture of having a nucleon nucleon scattering process with no influence of the residual nucleus  $A-1$  we can approximate  $\mathbf{p}_A \approx \mathbf{p}_i + \mathbf{p}_{A-1}$  where  $\mathbf{p}_i$  is the initial nucleon four-momentum inside the initial nucleus  $A$ . Since the initial nucleus is at rest ( $\mathbf{p}_A = 0$ ), the recoil momentum of the nucleus in final state  $\mathbf{p}_{A-1}$  equals to  $-\mathbf{p}_i$  the momentum of the initial nucleon pointing in opposite direction.

<sup>1</sup>In inverse kinematics the four-momentum vectors need to be boosted to the center of mass frame of the initial nucleus via Lorentz transformation.

In addition the four-momentum of the inner nucleon can be deduced from momentum measurement of the initial and final state nucleons:

$$P_i \approx P_{miss} \equiv P_1 + P_2 - P_0 \quad (4)$$

where  $P_{miss}$  is the so called "measured missing four-momentum of the reaction"<sup>[4]</sup><sup>2</sup>

Considering the momentum of the nucleus in the final state

### 2.2.2 Cross Sections for QFS Reactions - Qualitative Considerations

### 2.2.3 Application Fields of QFS Reactions

## 3 Experiment

The present commissioning experiment was performed in 2020 at the FAIR Facility at GSI (Gesellschaft für Schwerionenforschung) in Darmstadt (Germany). The GSI Helmholtzzentrum für Schwerionenforschung operates a unique accelerator facility for heavy ions and focuses on several cutting-edge research fields. These include:

1. **Nuclear Physics:** Studying the properties of atomic nuclei, exploring the forces that bind protons and neutrons, and investigating exotic nuclei far from stability.
2. **Hadron and Quark Matter:** Investigating the behavior of hadrons (particles made of quarks) and the state of matter under extreme conditions, such as those found in neutron stars or during the early universe.
3. **Atomic Physics:** Examining the structure and dynamics of atoms, including highly charged ions, to understand fundamental atomic interactions and refine quantum electrodynamics.
4. **Plasma Physics:** Creating and analyzing high-energy-density plasmas to simulate conditions found in stellar interiors and other astrophysical phenomena.
5. **Biophysics and Medical Research:** Exploring the effects of ion beams on biological systems for applications in cancer therapy, particularly using heavy ion therapy, and studying radiation protection for space missions.
6. **Materials Research:** Investigating the response of materials to high radiation doses to develop more resilient materials for use in various technologies, including nuclear reactors and space exploration.

---

<sup>2</sup> $P_{miss}$  is only equal to  $P_i$  for the unperturbed QFS (no ISI/FSI) case.

### 3.1 GSI facility

The GSI Helmholtzzentrum für Schwerionenforschung located at Darmstadt has a long history of research.... tell something about the beginnings, first really heavy elements found there.

The GSI Helmholtzzentrum für Schwerionenforschung GmbH was founded in 1969 (as "Gesellschaft für Schwerionenforschung mbH) looks back on a successful research history. In the time between 1981 and 2010 six new superheavy elements were discovered. In the medical research field GSI has developed advanced cancer therapy techniques using heavy ion beams which target tumors with high precision, minimizing damage to surrounding healthy tissues.

Along with those groundbreaking discoveries in research the facility at GSI has always been an inspiring source of drive for new technologies.

The key devices/apparatus which enable to carry out experiments with heavy ions at GSI are: important to mention: GSI is the only facility with heavy ions in the world. The starting point for the production of relativistic heavy ions at GSI is the ion source where ions are generated by stripping electrons off the shell of the atoms. Depending on the experimental needs the ion sources at GSI are able to produce ions of many different kinds of elements (up to Uranium).

On the first acceleration stage the stable primary ions are injected from the ion source into the UNIversal Linear Accelerator (UNILAC). On a length of 120 meters ions are accelerated up to maximum energy of 11.4 AMeV. The low energy beam is now injected into the ring accelerator SIS18 (Schwerionensynchotron 18). Here the ion beam is further accelerated up to 4.7 GeV/u (for protons) / 1 GeV/u (for Uranium). The magnets and the ultra-high vacuum ( $\sim 10^{-9}$  Pa) keep the ions well on their circular path (SIS18 has a circumference of 216 meters). For the production of rare heavy isotopes the primary ion beam from SIS18 can be impinged on a light nuclear target, e.g beryllium, the so called production target. These secondary beams of radioactive isotopes can be either stored in the experimental storage ring (ESR) for later use or transferred to the FRagment Separator (FRS). The FRS as a high-resolution magnetic spectrometer is capable to precisely select specific isotopes and to forward the desired beam of exotic relativistic nuclei to the various experiments or direct it to the ESR for later use.

#### 3.1.1 FAIR Project

The FAIR (Facility for Antiproton and Ion Research) situated next to the GSI will be one of the most complex and largest accelerator facilities in the world. The construction

of the superconducting ring accelerator SIS100 with a circumference of 1.1 km, storage rings and experiment sites begun in the summer of 2017. Commissioning is planned in 2025 (?). Early Science. Before the commmissioning of the ring accelerator SIS100 several prioritized experiments with large impact in the scientific world will take place in the newly built experimental halls, such as experiments with the R3BSetup in the High Energy Cave (HEC).

## 3.2 R3B Setup

The R3B (Reactions with Relativistic Radioactive Beams) experiment in Cave C at the GSI Helmholtz Centre for Heavy Ion Research in Germany is a cutting-edge research experiment focused on the study of nuclear reactions and structure using high-energy radioactive ion beams. The experiment aims to investigate exotic nuclei far from stability, offering insights into the fundamental properties of nuclear matter, nucleosynthesis processes, and the forces governing nuclear interactions. A schematic overview of the R3B Setup can be seen in Figure blabla.

The short living (neutron rich) isotopes are injected to the Cave C from the FRS, which preselects as mass spectrometer the isotopes of interest, and impinge on a fixed target. The R3B setup is designed for kinematically complete reaction studies. To fulfill this requirement the incoming ions are tracked and identified on an event-by-event basis by dedicated detectors in the FRS via time-of-flight and deltaE measurement techniques. Depending on the settings and composition of the incoming ion beam different type of reactions take place in the target area with a large variety of reaction products: heavy ions (as products from fission/spallation reactions), neutrons, light charged particles and gamma rays. For the detection of gammas and light charged ions from reactions with the target the dedicated CALIFA calorimeter (see more in section blabla) and various tracking detectors are installed in the target region. The GLAD (GSI Large Acceptance Dipole) magnet, located at the center of the Cave C, acts as mass spectrometer for the forward boosted charged reaction residues. The magnetic rigidity of the charged reaction residues is measured by a combination tracking detectors and a time of flight wall after the GLAD magnet. This allows to identify the charged reaction residues and their momenta. For the detection of the neutrons, not deflected by the magnetic field of the GLAD magnet, the new array neutron detector (NeuLAND) is positioned after GLAD on the zero degree line with the incoming ion beam.

The high flexibility of the R3B Setup, it can be operated with The combination of the large spectrum of incoming ion beams in a broad energy range provided by the FRS facility and the high flexibility of the R3B Setup with state of the art detectors for the

specific physics-studies of interest makes it to an attractive play-ground for experimental astro-physics.

### 3.3 Detector Setup in S444 Commissioning Experiment 2020

The S444 Experiment (successor experiment of the FAIR Phase-0 program in 2019, ref to Lukas Ponnath Thesis) for the commissioning of the CALIFA Calorimeter in its final mechanical design took place in February 2020. The choice to operate with stable  $^{12}\text{C}$  primary beam with four beam energy settings - 400/550/650/800 AMeV gave the opportunity to use it as preparation for the following up S467 experimental run with neutron-rich Ca isotopes as medium-heavy incoming beam. The detectors for positional tracking, charge identification and time measurement were provided by the SOFIA(Study on Fission with Aladin, make footnote that ALADIN was the predecessor or GLAD) collaboration. These detectors are optimized for fission experiments with medium to heavy reaction fragments. As for the S444 experiment with primary  $^{12}\text{C}$  incoming beam no fission reaction with multiple heavy charged fragments is expected the Sofia detectors were adapted accordingly (e.g. only one of the four sections of the Twin-Music Ionisation chamber was operated, see more in chapter Twin).

For this commissioning experiment most detectors and parts of the setup were operated in air. The target chamber was evacuated by gaseous helium at room temperature as well as the GLAD magnet. The fact that the ions interact with particles in air causes angular straggling in the flightpath reconstruction and can limit the resolution of reconstructed momenta from the reaction on the target.

#### 3.3.1 Multi Wire Proportional Chambers (MWPC)

The positional tracking of the incoming ions as well as the charged reaction products were performed by using Multi Wire Proportional Chambers (MWPC). A MWPC operates on the principle of proportional counters that are arranged side by side in a plane, thereby providing spatial resolution for particle radiation. The multi wire proportional chambers were developed in late 1960s by George Charpak<sup>3</sup> at CERN[5].

The MWPC operates in the same way as aligned proportional counters with the difference of not having dividing walls between the anode wires. This reduces the material budget, hence improving the spatial resolution and reducing reactions with the detected particle.

---

<sup>3</sup>George Charpak received the Nobel Prize in Physics in 1992 for his invention and development of particle detectors, in particular, the multiwire proportional chambers.

In the general design the MWCP is made up of a plane of anode wires enclosed between two cathode planes which are aligned parallel or vertical to the anode wires. Depending on the beam conditions the anode wires are set to high voltage ( $\sim 1100$  V) while the cathode planes are grounded.

The volume between the two cathode planes is filled by a gas mixture of 84% Argon and 16% CO<sub>2</sub>. The decision of the gas mixture is driven by a balanced ratio between amplification and quenching properties of the gas.

When a charged particle passes through the detector it ionizes the gas. Primary electrons are created followed by a secondary ionization via electron avalanche. The electron avalanche drifts towards the wires (anodes) while the positive ions drift towards the grounded cathode planes. As the MWPCs are operated in the proportional region, the number of created electrons/ions is proportional to the initial ionization. Instead of reading out the signal from the wires it is read out from the strips of the cathode plane. This improves the position resolution in case the cathode planes are aligned perpendicular to the wires. In case multiple (neighboring) strips give signal the signal distribution over the strips is analyzed and fitted to provide the position information.

In the R3B setup for the S444 experiment four MWPCs were installed:

1. MWPC0: right at the beginning of the beam entrance in Cave C, 184 cm upstream to the target position to detect x- and y positions of the incoming ions.
2. MWPC1: 88 cm downstream to the target for positional tracking in x and y of the outgoing reaction fragment
3. MWPC2: 154 cm downstream also for positional tracking of the fragment
4. MWPC3: after the GLAD magnet. The x position of this detector gives the information about the magnetic rigidity of the reaction fragment.

Despite having the same mode of operation, they slightly differ in their construction design and positional resolution. For the technical specifications of the individual MWPCs, see table 1. Still to do: put in plot with potential field of mwpc and one with crosssign charged particle.

### 3.3.2 Ionisation Chambers - R3BMusic/TWIM Music

For the S444 experiment at R3B two types of multi sampling ionisation chambers (MUSICs) were installed: the R3B MUSIC, centered 153 cm upstream to the target, and the TWIN-MUSIC, 132 cm downstream to the target. Like the MWPCs (see

<b>Common MWPC Settings</b>	
Gas	84% Ar, 16% CO <sub>2</sub>
Windows	Mylar®
Anode wires voltage	1100 V
Cathode planes voltage	Ground
Wire pitch	2.5 mm
Wire diameter	5 μm
Width of X pads	3.125 mm

<b>MWPC0</b>	
X pads	64 pads, vertically segmented into two equal parts
Y pads	64 pads, horizontally segmented (3.125 mm width)
Active surface	200 × 200 mm <sup>2</sup>

<b>MWPC1 &amp; MWPC2</b>	
X pads	64 pads, vertically segmented into two equal parts
Y pads	40 pads (5 mm width), horizontally segmented
Active surface	200 × 200 mm <sup>2</sup>

<b>MWPC3</b>	
X pads	288 pads
Y pads	120 pads (5 mm width)
Active surface	900 × 600 mm <sup>2</sup>

Table 1: SOFIA MWPCs - Technical specifications

3.3.1) the ionisation chambers are gas-filled detectors for tracking down charged particles. While MWPCs consist only of a few mm of active gaseous volume, the ionsiation chambers have an expanded gaseous volume which allows to make precise energy loss measurements from the ionisation process of the gas. The multi sampling ionsiation chambers consist of a cathode plane and an anode plane, consisting of multiple anode strips. When a charged particle crosses the chamber the gas gets ionized and the created electrons and ions are separated by the strong electric field. While the ions drift towards the cathode plane the electons move to the anodes where each anode is read out separately. Since the energy loss of the passing through particle is proportional to the square of its charge ( $\Delta E \sim Z^2$ ) the signal from the anodes allow to precisely measure the charge of the particle. Moreover multi-sampling ionisation chambers measure the drift time of the electrons created during the ionisation process on each anode (com-

pared to one or more reference anodes). Assuming a constant electron drift velocity ( $\sim 40\text{mm}/\mu\text{s}$ ) over the gaseous volume the time information of each anode signal can be used to reconstruct the x-position of the passing through particle).

### R3B MUSIC

The R3B MUSIC, installed 153 cm upstream to the target, is used to measure both the charge of the incoming ion before impinging on the target and the angle of the particle's trajectory. The detector has an active gaseous dimension of  $20 \times 20 \times 40 \text{ cm}^3$ , confined on one side by a cathode plane and on the other side by an anode plane consisting of 10 anodes ( 8 readout anodes and 2 screen anodes). For the technical specifications, see table 2.

---

<b>Dimensions</b>	
Detector dimension:	$51 \times 54 \times 53 \text{ cm}^3$
Active dimension:	$20 \times 20 \times 40 \text{ cm}^3$
Dimension of one anode:	$20 \times 20 \times 5 \text{ cm}^3$
Dimension of one screen anode:	$20 \times 20 \times 2 \text{ cm}^3$
<b>Gas</b>	
P75 (Ar 25%, CH <sub>4</sub> 75%)	
<b>Voltage</b>	
Cathode (left to beam direction):	-(2 – 6)kV
Anode (right to beam direction):	+300V
<b>Resolutions</b>	
still to do!	

---

Table 2: R3B MUSIC - Technical specifications

### TWIN MUSIC

The TWIN MUSIC is a double ionisation chamber with one central cathode plane and two independent drift volumes and anode planes on each side. Each of the anode planes consists of 16 anodes for readout plus two screen anodes. Furthermore each anode is again segmented into up/down which splits the detector into four dedicated sections. As the TWIN MUSIC is placed 132 cm downstream to the target it is employed to measure charge and angular direction of the outgoing medium-to-heavy fragments. The detector was in particular designed for fission experiments where two or more fission fragments are created. If each fragment is flying through one of the four sections ( which is mostly the case due to momentum conservation rules) charge and angle of each fragment can be measured independently.

To fulfill the required permanence of the field in both extended gaseous volumes (of

dimension 11x22x40 cm<sup>3</sup>) a Frisch grid is located 3 mm from the anode planes. The Frisch grid is metal mesh grid that shields the anode from the movement of ions produced during ionization process in the chamber ensuring that only the electrons that reach the anode contribute to the signal. Additionally, the shielding of the anodes by the Frisch grid account for the fast rise time of the signal at the anodes which diminishes pile-up effects and makes the detector high beam-rate capable (up to 100kHz). Further technical specifications you can find in table (bla bla)

---

### Dimensions

Detector dimension:	43 x48 x55 cm <sup>3</sup>
Active dimension:	two halves each 11x22x40 cm <sup>3</sup>
Distance central cathode - Frisch grid:	11 cm
Distance Frisch grid from anode planes:	3mm

### Gas

CH4 [79%], Ar [20%] and CO2 [1%]

### Voltage

Central cathode:	-(2 – 6)kV
Anode planes:	+600V
Frisch Grid:	+250V

### Resolutions

$\Delta E/E$	< 5% FWHM, total < 2% FWHM
$\Delta X$	< 40 $\mu$ m

---

Table 3: TWIN MUSIC - Technical specifications, see also [6]

### 3.3.3 Sofia Start Detector

The SOFIA Start detector is positioned right after the R3B Music ionisation chamber and gives a time reference for the incoming ion. It is a 1 mm thin scintillating plastic blade attached with a photo multiplier tube on each side. The scintillator light from excitation of the incoming ions produce a clear signal on both photomultiplier tubes used for the time measurement:

$$t_{start} = 0.5 \cdot (t_{left} + t_{right})$$

To shield the plastic detector from daylight it is wrapped in mylar foil (300 $\mu$ m thickness).

### 3.3.4 GLAD Magnet

The **GSI Large Acceptance zero degree superconducting Dipole magnet GLAD** sits in the center of the R3B Setup in the cave C hall<sup>2</sup>. With an adjustable field integral up to 5 Tm it has a high acceptance range in magnetic rigidity which is crucial for the identification of highly asymmetric reaction fragments. The homogeneous magnetic field in GLAD allows to achieve momentum resolutions  $\Delta p / p$  of  $10^{-3}$  in combination with the dedicated tracking system.

The large opening angle of  $\pm 80$  mrad makes the GLAD magnet highly transmissive for evaporated or scattered neutrons in the reaction process which will be subsequently detected in the NeuLAND detector.

The default bending angle of the beam with respect to the beam line was set to  $18^\circ$ . Herefore the currents where adjusted according to the beam energy:

1. 400 AMeV beam: 1444 Ampere
2. 550 AMeV beam: 1778 Ampere
3. 650 AMeV beam: 1957 Ampere
4. 800 AMeV beam: 2223 Ampere



Figure 2: Upstream view of GLAD magnet in the center of Cave C after installation in February 2016. Picture from [7]

### 3.3.5 CALIFA Calorimeter

The **CALOrimeter for In Flight detection of  $\gamma$ -rays and high energy charged pArticles**, CALIFA, is one of the main detector components of the R3B setup. It surrounds the target area and covers the full azimuthal range and a polar angular acceptance from

$7^\circ$  up to  $140^\circ$  in the target region. The calorimeter serves for the detection of gamma rays in the energy region  $100 \text{ keV} \lesssim E_\gamma \lesssim 30 \text{ MeV}$  and light charged particles, mostly protons, up to  $E_p \lesssim 700 \text{ MeV}$ . To fulfill the demands requested by the different experimental campaigns an energy resolution of  $\frac{\Delta E}{E}(@1\text{MeV}) \sim 6\%$  in the gamma-ray energy regime  $\frac{\Delta E}{E}(@100\text{MeV}) \sim 1\%$  in the proton range regime is required.

### Geometry

The CALIFA detector is a highly segmented detector with more than 2500 CsI crystals installed in the final design. Since experiments in the R3B setup operate in relativistic kinematics both the incoming ions as well as the measured particles originating from reactions inside the source experience relativistic effects, more precisely the so called relativistic Doppler effect. The emitted gammas and protons are not isotropically distributed around the source region but are boosted in forward direction. Moreover, the energy measured in the lab frame is different from the kinetic energy in the rest frame of the incoming ion.

The relativistic Doppler effect has a huge impact on the geometric design and requirements of CALIFA. Therefore the detector was subdivided into three polar angle ranges<sup>3</sup>:

- $7^\circ \leq \theta \leq 19^\circ$  - CEPA (CALIFA Endcap Phoswich Array): The most forward segment consists of 96 CsI(Tl) crystals. Due to the aforementioned rel. Doppler effect this area will have the highest intensities and energies. For high beam energies most of the particles will not be stopped inside the crystal and will escape as "punch-throughs". Despite the "punch-through" ions deposit only a fraction of their kinetic energy ( $\Delta E$ ) in CALIFA it is possible to reconstruct the initial energy of the particle<sup>4</sup>. In CEPA crystals with a length of 15 cm are used and cover each a polar angle of  $\approx 2^\circ$ . This finer segmentation in polar angular range has the benefit to compensate for the high rate.
- $19^\circ \leq \theta \leq 43^\circ$  - Intrinsic Phoswich (iPhos): In conjunction with the CEPA, the iPhos region forms a part of the CALIFA Endcap. The iPhos region is, same as for the CEPA, affected by high rates. Protons reaching this region have high kinetic energies ( $E_{kin,p} \leq 600 \text{ MeV}$ ) and therefore a large fraction of "punch-throughs" are expected. In the iPhos region 480 CsI(Tl) crystals with a length of 22 cm<sup>5</sup> are

---

<sup>4</sup>This is done by exploiting the distinct scintillation components of CsI, see more in chapter 5 of [9]

<sup>5</sup>To fully stop protons with  $E_{kin,p} \approx 600 \text{ AMeV}$  crystals with a length of 60 cm would be needed.

Such long crystals would have multiple drawbacks: reduced energy resolution due to worse scintillator light transport, enhanced nuclear reactions inside the crystals and challenging demands on stability of

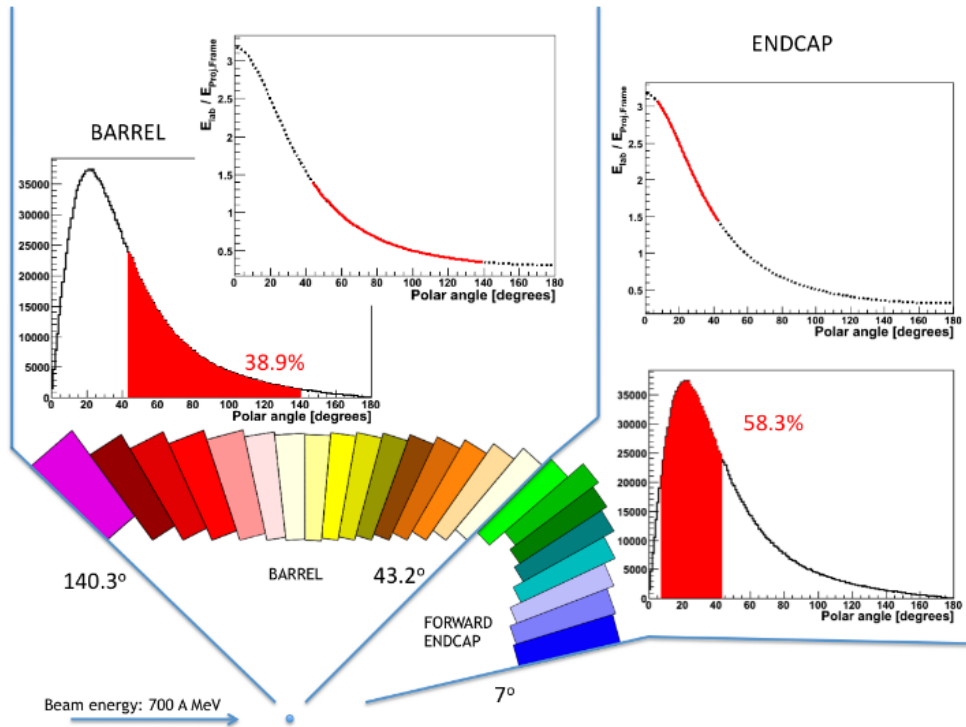


Figure 3: Schematic view of the Barrel and Endcap(iPhos and CEPA) segments of CALIFA and the according angular and energy distribution of emitted  $\gamma$  rays (monoenergetic in the projectile frame at beam energy of 700 AMeV). From [8]

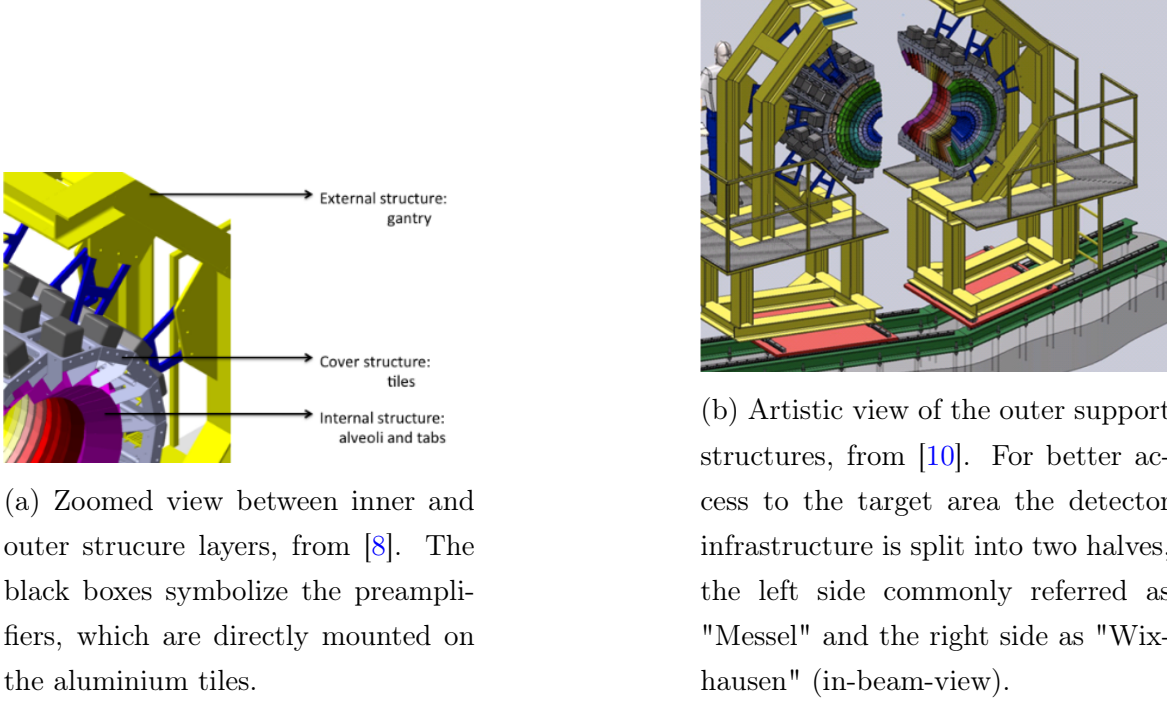


Figure 4: CALIFA internal and external holding structure

installed and cover each a polar angle of  $\approx 3^\circ$ . (For more information see Endcap TDR:[10]).

- $43^\circ \leq \theta \leq 140^\circ$  - Barrel: This segment covers the region where the lowest rates and energies are expected. The Barrel region contains 1952 CsI(Tl) crystals, due to the large polar angular coverage and the requirement of Doppler correction via angle measurement. The most forward crystals have a length of 22 cm (which allow to stop protons with  $E_{kin,p} \leq 315\text{MeV}$ ). This length is reduced down to 12 cm for the most backward crystals (For more information see Barrel TDR:[8]).

The crystals are arranged in carbon fibre alveoli with a nominal wall thickness of 230  $\mu\text{m}$ [8] that provide a support structure for the crystals and keep the material budget as low as possible. The alveoli in turn are hold and covered by individual aluminium tiles. The volume enclosed by the alveoli and the aluminium tiles is flooded with nitrogen to keep humidity low on the surface of the crystals. For a sufficient suspension of the aluminium cover a robust external holding structure was designed.

In 2019 CALIFA was for the first time integrated into the R3B setup in form of the CALIFA demonstrator, a prototype consisting of seven mechanically separate petals, each of it containing a set of 64 crystals.

At the end of 2019 the CALIFA frame in its final design was installed and the forward

---

the detector holding structure

barrel part ( $43^\circ \leq \theta \leq 90^\circ$  and full azimuthal coverage) was equipped with 1024 crystals.

For the S444 and the S467 experiment in 2020 CALIFA was equipped with 180 more crystals in the iPhos region ( $19^\circ \leq \theta \leq 43^\circ$ ) which corresponds a coverage of 37.5 % in azimuthal angle for that region. Right before the S455 fissioning experiment [11] the full installation of the iPhos region was completed.

In February 2024 the full CEPA region ( $7^\circ \leq \theta \leq 19^\circ$ ) with 96 crystals was commissioned for the first time together with a new equipped part of the backward barrel ( $90^\circ \leq \theta \leq 102.5^\circ$ , 128 crystals).

### Energy and particle reconstruction with CsI scintillator crystals

Scintillator material, as caesium iodide doped with thallium (CsI(Tl)), is widely used in experimental physics to detect ionizing radiation from  $\gamma$ -rays or charged particles. The energy from the incoming radiation excites the electrons in the CsI crystal from their ground state to higher energy levels (excited states). The deexcitation, followed by photon emission (scintillation light), occurs via various complex mechanisms, not all of them completely understood yet (for more information see TODO:references!). The efficiency and properties of the scintillation process can be fine-tuned by doping CsI with small amounts of other materials, such as thallium. Thallium-doped Cesium Iodide produces light with a peak emission around 550 nm (green light) and has high light output<sup>6</sup>. The high density of CsI with  $4.51 \text{ g/cm}^3$  makes it to an optimal scintillator material to efficiently absorb  $\gamma$ -rays and other high-energy particles. Moreover the CsI(Tl) crystal is well transparent to its own scintillation light, which is essential for the detection of the scintillator light. CsI(Tl) crystals are in addition relatively robust compared to other crystals and only slightly hygroscopic making them suitable for long-term use in experimental setups.

In a first approximation, the total amount of emitted light is proportional to the energy deposited in the scintillator. For  $\gamma$ -rays this is valid for  $E_\gamma \gtrsim 400 \text{ keV}$ [13]. However, for charged particles significant deviations from linearity are observed, a so called "quenching" (TODO: add here more information, also the thesis of Max Winkel).

Although the energy calibration of CsI(Tl) crystals for charged particles is challenging, CsI(Tl) as such has the beneficial property of having a complex time dependent light emission consisting of two distinct exponential components. The time dependent light emission response of CsI(Tl)  $L(t)$  can be approximated as:

$$L(t) = \frac{N_f}{\tau_s} \exp(-\frac{t}{\tau_f}) + \frac{N_s}{\tau_s} \exp(-\frac{t}{\tau_s}) \quad (5)$$

Where  $N_f$  is the amplitude of the fast component and  $N_s$  the amplitude of the slow

---

<sup>6</sup>The light output per MeV deposited energy in CsI(Tl), measured in [12], resulted in  $5.2 \cdot 10^4$  (scintillation) photons/MeV.

component. Accordingly  $\tau_f$  the life time of the fast component ( $\tau_f \approx 650 - 770\text{ns}$ ) and  $\tau_s$  the lifetime of the slow component ( $\tau_s \approx 3.2 - 3.5\mu\text{s}$ ). It has been found that the proportion between the two components is energy and particle dependend. This property can be used to identify isotopes by extracting the  $N_f$  and  $N_s$  values from pulse shape analysis (PSA) on the according light emission response<sup>7</sup>. TODO: put in a picture of nf vs ns an one with the scintillation light impulse

### From scintillator light to electrical signal

The scintillator light produced by the ionisation processes has first to be transported to the back-end of the crystal. The optimum design has been determined to be frustum-shaped crystals, wrapped into enhanced specular reflector (ESR) foil which provides excellent reflectivity. Finally at the backside of the crystals a large area avalanche photodiode (LAAPD) is attached<sup>8</sup>. Avalanche photodiodes have the same working principle as photodiodes to convert (scintillator) light into electricity. As a result of an additional highly doted p-layer a region with very high field is formed which accounts for amplification factors up to  $\approx 100$ .

For the next amplification step the electric signal is forwarded via thin ribbon cables to the back end of the preamplifiers from Mesytec[17] which can serve up to 32 input channels. For CALIFA two general types of peramplifiers are in use:

1. Dual Range (DR) Preamplifiers: They are used in the iPhos and CEPA region where both high energetic protons as well as gammas are expected. They cover two amplification ranges in parallel: the *gamma range* with low input signal and high amplification and the *proton range* with high input signal with low amplification. Following from this they have 64 channel differential signal output.
2. Single Range (SR) Preamplifiers: In the Barrel region, where mostly  $\gamma$  rays are expected, only one amplification range is needed. Depending on the experimental demands these preamplifiers can be switched to *gamma* or *proton range*. These peamplifiers have a 32 channel differential signal output.

The fall time for the preamplifiers  $\tau_{RC}$  has been chosen to  $\approx 35\ \mu\text{s}$ . This is a trade-off between the ballistic deficit on one side (reduction of the signal amplitude due to low  $\tau_{RC}$ , see also [14], chapter 3.4.5) and rate capability (restricted by large  $\tau_{RC}$  value) on the other side.

The differential signal output of the preamplifiers is then transmitted over shielded and twisted line pairs to the input of the FEBEX Addon Boards (FAB) for further processing.

---

<sup>7</sup>The method has been implemented in the CALIFA Firmware as *QuickParticleIdentification – QPID*. For more information see [14] and [15]

<sup>8</sup>Detailed information about the crystal wrapping and LAAPD gluing can be found in this work:[16]

## Signal Processing and readout system

The central hardware module for the signal processing in CALIFA is the FEBEX 3B Module (Front End Board with optical link EXtension[18]). Attached on it is a so-called AddOn board developed by TUM. The signal from the preamplifier gets here first filtered by a low pass two pole bessel filter ( $f_c \approx 25MHz$ ). Furthermore, since the input of the FEBEX ADCs cover a range of  $\pm 0.9$  V while the signal output from the preamplifier only has one polarity, an offset to the signal is applied to use the full range of the ADCs. The signal from the ADCs is read out continuously on the FEBEX card and split up into two branches:

1. Fast/trigger branch: After being fed to a trapezoidal filter the signal is examined by three leading edge discriminators with configurable thresholds. Depending on the experimental requirements a coincident matrix between one or more discriminators and optionally external triggers validates the signal as event ready for data recording.
2. Slow branch: The validated signal gets delayed over a ring buffer and a pulse shape analysis is performed via various steps - signal decimation, moving average unit -technique, baseline subtraction and moving window deconvolution (MWD) - to recall the major steps<sup>9</sup>. From the resulting pulse shape pulse height measurement the energy deposited in the scintillator is determined. In addition the algorithm for the quick particle identification (QPID) is applied on the incoming signal which provides the fast( $N_f$ ) and slow( $N_s$ ) component of the signal for isotope identification and differentiation of stopped and punch-through particles. The CALIFA Firmware also allows to make time over threshold (TOT) measurements which is convenient for energy reconstruction when the incoming signals exceed the ADC range (which might happen when the preamplifier is set to *gamma range*)<sup>10</sup>.

Central hub for internal and external trigger forwarding are the Exploder modules[20]. The FEBEX crates are connected over an eight fold flat cable to the Exploder to the triggerbus. The trigger bus between the data acquisition PCs and the FEBEX cards is controlled by the TRIXOR card. This card sits inside the data acquisition PCs and is connected via ECL-lines to the Exploders and the PEXOR(PCIe Optical Link Interface) card via 26 fold flat cable. The PEXOR card is responsible for the data transfer

---

<sup>9</sup>A really detailed description of the pulse shape analysis in CALIFA can be found in Philipp Klenze's[19] and Max Winkel's thesis[15].

<sup>10</sup>The TOT energy-reconstruction method has the drawback of being really sensitive to pile-up events overestimating the energy deposition. Hence more suitable for regions with low event rates, such as Barrel region.

between FEBEX cards and the data acquisition PCs. It is connected via glass fibre cables to the FEBEX crates and stores locally in a 576 MB large RLDRAM (Reduced Latency Dynamic Random Access Memory) the data which consecutively gets transmitted via DMA (Direct Memory Access - data transmission speed up to 560 MB/s) to the RAM of the data acquisition PCs.

Since the Exploder provides various input and output lines and an internal switchable bypass matrix the CALIFA calorimeter can be operated as free running system with internal event validation only or by (additional) external validation. In case of internal validation only the signal from the preamplifiers has to exceed predefined threshold(s) to be accepted. This kind of configuration can be used for the purpose of calibration (with  $\gamma$ -ray sources like  $^{22}\text{Na}$  or  $^{60}\text{Co}$ ) and expected low event rate experiments. For high event rates and event coincidence with other subdetectors additional external validation (e.g. clean CFD signal from START detector) is implemented.

To overcome dead time initiated by the readout/data transmission procedure each FEBEX channel allows to store up to 254 recorded events on the local memory. Each FEBEX channel has two available memory banks. Whenever one FEBEX channel reaches its preconfigured maximum number of events the full FEBEX crate is read out. To avoid dead time all channels force a memory bank switch thus allowing continuous dead time free event recording.

The Multi Branch System (MBS), developed at the GSI Helmholtz Center for Heavy Ion Research, is used on the data acquisition PCs. This software consists of several components that control and read out detectors, store the data, or forward it via various network protocols. The system also allows for the joint readout of multiple systems. For this, the trigger modules (TRIXOR) are connected via a special trigger bus to exchange trigger signals and dead time information. The triggered data is then collected, time sorted and cross-detector events are built by the dedicated MBS event builder<sup>11</sup>.

### 3.3.6 Sofia Time of Flight Wall

The Sofia Time of Flight Wall (or "Stop detector") is positioned at the very end of the experiment setup at approximately 6.6 m distance from the target position. It consists of a plane of 28 vertically aligned scintillator bars, each of dimension 32x600x5 mm. The scintillator plastics are numbered from 0 to 28 from left to right (when looking in beam direction). The time of flight of the ions between Start and ToFW can be measured by subtracting the time measurement of the Start detector from the ToFW. The combined resolution of the Start and TOFW detector is at 40 ps, for an average

---

<sup>11</sup>A more detailed explanation about the readout system and the critical FEBEX timing topic can be found in Philipp Klenze's thesis [19].



Figure 5: Sofia ToFW in Cave C, from [6].

Plastic	EJ-232, no quencher
Plastic dimensions	5x32x600 mm <sup>3</sup>
Detector dimension	5x900x600 mm <sup>3</sup> (28 plastics)
Photo-multiplier tubes	Hamamatsu 6533 and 10580
Total number of PMTs	56 (two per plastic - top and bottom)

Table 4: Sofia ToFW - Technical specifications

time of flight of 30 ns[6]. For the technical specifications of the Sofia ToFW, see table 4 and reference [21].

### 3.3.7 NeuLAND Detector

For the detection of knocked-out or evaporated neutrons the **New Large-Area Neutron Detector (NeuLAND)** is installed at zero degrees after GLAD. In its final design it will consist of 30 double planes with 100 plastic scintillators of size 5x5x250 cm<sup>3</sup> providing an active detector surface of 2.5x2.5 m<sup>2</sup> and thickness of 3m. Its high detection efficiency, a time resolution of  $\sigma_t \leq 150\text{ps}$  and a mult-neutron efficiency of 50% to 70% for four-neutron events are crucial detector features for complete kinematics experiments at R3B. For more detailed information, see [22] and [23].

For the S444 commissioning experiment in 2020 eight double-planes of the NeuLAND detector have been used.

### 3.3.8 Calibration of the Detector Systems

## 4 Analysis - Total Interaction Cross Section of $^{12}\text{C}$ + $^{12}\text{C}$

This chapter will go through the analysis step by step from the unpacking stage to the final measurement of the total interaction cross section. It will start by a short overview of the transmission method used for the cross section measurements. The next step is the selection of clean incoming  $^{12}\text{C}$  isotopes. Following the identification of the carbon isotopes after the target - for the measurement of the charge changing cross section - and as final step the interaction cross section measurement.

All relevant detector related geometrical and efficiency corrections will be addressed and their influence to the final result and its uncertainty will be discussed.

### 4.1 Cross Section Measurement via Transmission Method

In its most generic form cross sections give a measure of the probability that a specific reaction will take place when two or more particles collide. The cross sections measured in scattering experiments, as well as the energy and angular distribution of the reaction products, provide information about the dynamics of the interaction between the projectile and the target particle, i.e., about the shape of the interaction potential and the coupling strength.

The cross section  $\sigma$  can be derived by looking at the relation between the number of incoming particles ( $N_1$ ) and unreacted particles after the target ( $N_2$ ). For an experiment with fixed target with thickness  $z$  and volumetric number density  $n$  the number of reacted particles in the infinitesimal thin target layer  $dz$  can be expressed as:

$$\frac{dN_2}{dz} = -n\sigma N_2 \quad (6)$$

Solving this differential equation for  $N_2$  (with the condition  $N_2 = N_1$  for  $z = 0$ ) discloses an exponential relation:

$$N_2 = N_1 e^{-n\sigma z} = N_1 e^{-N_t \sigma} \quad (7)$$

Where  $n \cdot z$  can be summarized as  $N_t$ , the total number of scattering centers per unit area. The relation  $(N_2/N_1)$ , number of unreacted particles after the target versus number of incoming particles, is often called survival probability  $P_{surv}$ . For an idealistic experimental setup with full detector efficiency and no interactions in the setup material the cross section could simply be deduced from equation 7. To account for reactions of the projectile that occur within the setup material and first order detector specific distortions of output signals the survival probability  $(N_2/N_1)$  has to be divided by the survival probability for an empty target run  $P_{surv}^E = (N_2^E/N_1^E)$ , where  $N_1^E$  is the number

of incoming particles and  $N_2^E$  the number of unreacted particles after the target for an empty run respectively. Thereby the setup specific efficiency( $\epsilon_{setup}$ ) and transmission factor( $t_{setup}$ ) are cancelled out to obtain the underlying number of unreacted particles after the target  $\tilde{N}_2$ :

$$N_2 = \tilde{N}_2 \cdot t_{setup} \cdot \epsilon_{setup}, \text{ with } \tilde{N}_2$$

$$N_2^E = \tilde{N}_2^E \cdot \epsilon_{setup} \text{ with } \frac{\tilde{N}_2^E}{N_1^E} \text{ the setup specific transmission factor } t_{setup}$$

The final formula for the cross section for a so called transmission measurement is:

$$\begin{aligned} \sigma &= -\frac{1}{N_t} \ln\left(\frac{N_1^E}{N_2^E} \cdot \frac{N_2}{N_1}\right) = -\frac{1}{N_t} \ln\left(\frac{N_1^E}{\tilde{N}_2^E \cdot \epsilon_{setup}} \cdot \frac{\tilde{N}_2 \cdot t_{setup} \cdot \epsilon_{setup}}{N_1}\right) \\ &\quad \text{With } \frac{\tilde{N}_2^E}{N_1^E} = t_{setup} \quad (8) \\ \sigma &= -\frac{1}{N_t} \ln\left(\frac{1}{t_{setup}} \cdot \frac{\tilde{N}_2 \cdot t_{setup}}{N_1}\right) = -\frac{1}{N_t} \ln\left(\frac{\tilde{N}_2}{N_1}\right) \end{aligned}$$

From the above formula 8 it is evident that for cross section measurements with the transmission method three types of observables have to be measured:

## ■ Number of scattering centers $N_t$

The number of scattering centers per unit area of the target is a target specific number. It depends from the target thickness and and its density. The values herefore are taken from [24]<sup>12</sup>:

(a) Thin target:

target thickness  $d = 0.5451 \text{ cm}$ ;  $N_t = 5.0588795 \cdot 10^{22}$ ;  $\Delta N_t = 0.0648\%$

(b) Medium target:

target thickness  $d = 1.0793 \text{ cm}$ ;  $N_t = 1.0016600 \cdot 10^{23}$ ;  $\Delta N_t = 0.2620\%$

(c) Thick target:

target thickness  $d = 2.1928 \text{ cm}$ ;  $N_t = 2.0350598 \cdot 10^{23}$ ;  $\Delta N_t = 0.0322\%$

where  $N_t$  was calculated by:

$$N_t = \frac{\rho \cdot d \cdot N_A}{M} \quad (9)$$

with  $\rho$  the target density<sup>13</sup>,  $N_A$  the Avogadro constant ( $6.02214076 \cdot 10^{23} \text{ mol}^{-1}$ ) and  $M$  the molar mass of the target (for carbon  $M = 12.011 \text{ g} \cdot \text{mol}^{-1}$ ).

---

<sup>12</sup>For the purpose of this work the target thicknesses were remeasured at GSI with a chromatic sensor giving 2D depth profiles of each target.

<sup>13</sup> $\rho = 1.851 \text{ g/cm}^3$ , from [24]

### ■ Number of incoming projectiles ( $^{12}\text{C}$ ) $N_1$

For the measurement only events with well identified incoming  $^{12}\text{C}$  projectiles are chosen. Therefore strict cuts on the detectors upstream the target area are set. This strict event selection makes sure that we only consider events with single  $^{12}\text{C}$ . This will be discussed in more detail in section 4.2.

### ■ Number of unreacted projectiles ( $^{12}\text{C}$ ) $N_2$ after the target

Detectors downstream the target area are used to count the number of unreacted projectiles  $^{12}\text{C}$ . To reduce detector specific influences which could distort the result it is advisable to use only as few as required detectors for the clear identification of unreacted projectiles. Moreover detector specific efficiencies are cancelled out by including both empty and target runs in the cross section calculation(see equation8). For all downstream detectors used in this analysis it is critical to minimize any selection cuts and systematically check their effects on  $N_2$ .

## 4.2 Event Selection

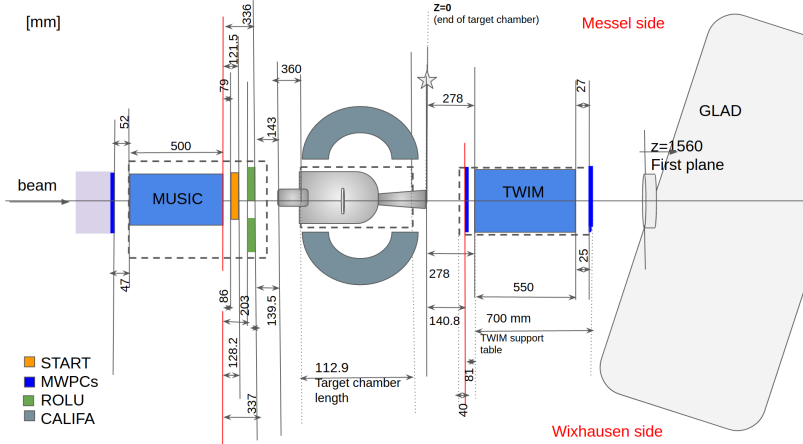


Figure 6: R3B Setup for the S444 experiment in the target region. TODO: select overview with less numbers/measures...

For event selection, all three upstream detectors are utilized: the MWPC0, the R3BMUSIC Ionization Chamber, and the start detector. To ensure a clean incoming event selection, the following prerequisites must be met:

#### 1. $^{12}\text{C}$ identification of incoming projectile by upstream detectors:

In the S444 experiment the incoming beam was directly delivered by the SIS18 ring accelerator, which is operated in ultra-high vacuum. The level of contamination is low.(TODO: up to which stage do we have vacuum? Until MW0?)

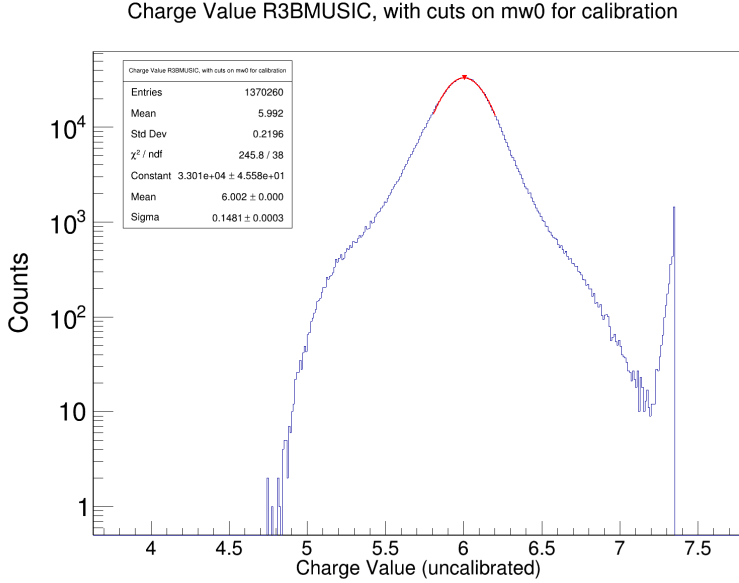


Figure 7: Charge distribution on R3BMUSIC with predefined calibration parameters with already applied positional cuts on MWPC0 - positioned upstream to the ionisation chamber. The rise beyond  $Z \geq 7.2$  comes from pile-up events. TODO: more explanation needed? 2D plot needed?

For the charge identification of the incoming ion the R3BMUSIC ionisation chamber is used which is positioned directly after the MWPC0 at the beam entrance in Cave C, see figure 6. The R3BMUSIC detector measures anode-wise the energy loss of the passing-through ion which in the first order is proportional to the square of its charge ( $\Delta E \sim Z^2$ ). Therefore the calibration parameters from the online analysis are used<sup>14</sup>. Figure 7 shows the measured charge distribution in R3BMUSIC. To select  $Z = 6$  incoming ions the distribution is fitted with a gaussian fit function. All ions with charge within the  $\pm 1\sigma$  range are accepted. Figure 8 summarizes the  $\pm 1\sigma$  cuts on the R3BMUSIC charge for empty/target runs for all beam energies.

## 2. Pileup rejection and TPat selection:

The overall recoding and merging of the data from various subdetectors is one of the tasks of the Data AcQuisition (DAQ) system. Whether an event is recorded or not depends on the pre-established trigger logic. Various detectors can send out triggers to the main DAQ when certain conditions are given (e.g. CALIFA can be configured to send out a trigger when a hit with more than 20 MeV is recorded in the calorimeter). The different triggers are processed by the trigger logic and summarized as a defined trigger pattern, so called TPat, which is stored

<sup>14</sup>These are generic parameter values used to the detector performance during the experiment phase.

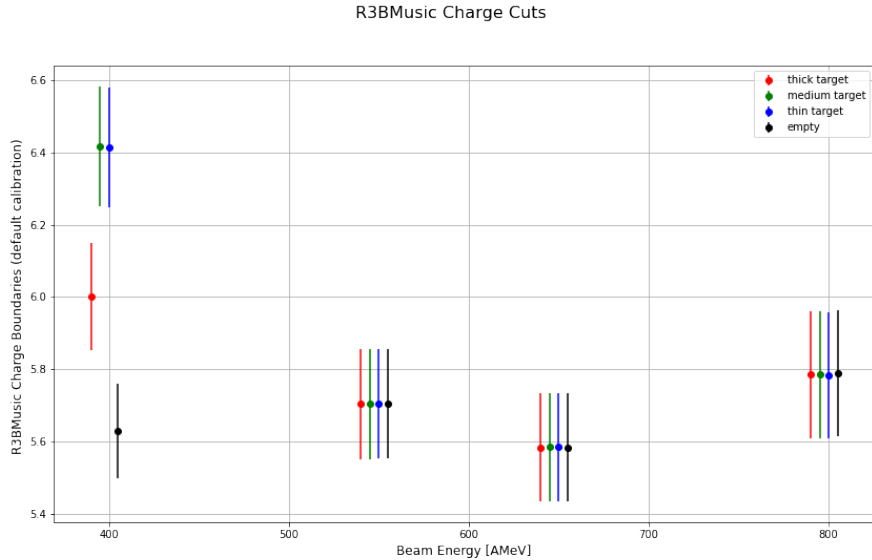


Figure 8: Strict  $\pm 1\sigma$  charge cuts with R3BMUSIC for incoming particle selection. Fixed predefined calibration parameters were used which do not compensate different gain settings between runs. This is in particular the case for the 400 AMeV beam energy runs.

in a 16-bit mask for each event. Table 5 gives an overview of the trigger logic and the trigger patterns set in the S444 experiment. For this analysis the "*Min. Bias*" trigger is required<sup>15</sup>.

Since the TPat selection itself does not necessary set any pileup constraints it

Bit Position	TPat Name	Description
0	Min Bias	Hit in Start detector
1	Reaction	"CalifaOR" -high energy hit in CALIFA
2	Neutron	Hit in NeuLAND
3	p+n	Hit in CALIFA and Neuland
8	Califa	high energy hit in califa - off-spill
9	NeuLAND	Hit in NeuLAND - off-spill

Table 5: List of TPats set for S444 experiment. As for the selected runs low beam rates ( $< 10kHz$ ) were expected no dead time issues should arise for the in-beam detectors, therefore no downscaling of the *Min. Bias* TPat was deployed.

is important to analyse the signals of the detectors upstream carefully to insure

<sup>15</sup>This includes also "*Reaction*" and "*Neutron*" TPat since these patterns contain also "*Min. Bias*" TPat as necessary condition.

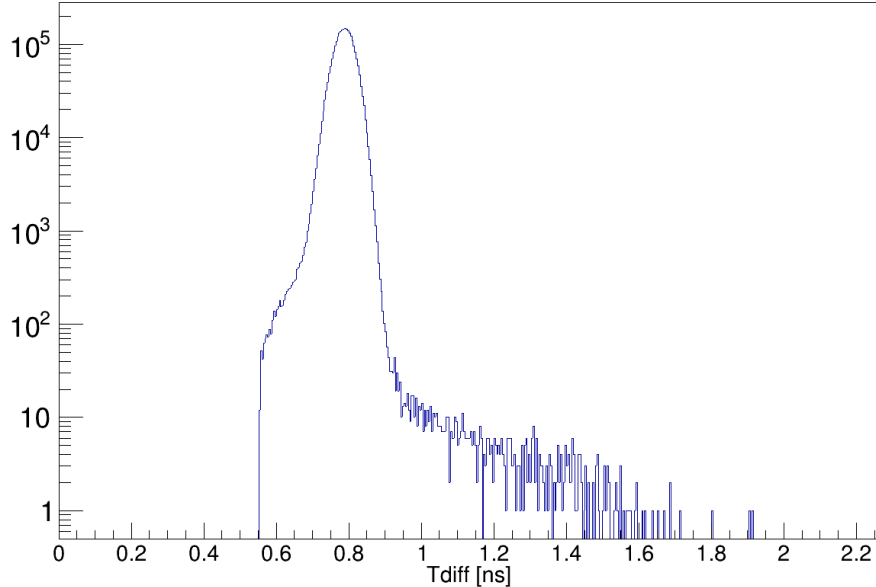


Figure 9:  $\Delta t_{\text{right-left}}$  between hits in the Start detector for events with exactly one hit on the left and right preamplifier and limiting the time difference in the range 0.555 ns to 1.946ns.

yourself that only events with one incoming  $^{12}\text{C}$  ion at a time get selected. Therefore events with incoming ions with charge  $Z = 6 \pm 1\sigma$  are chosen, as discussed in the previous point. Moreover it is required that both left and right preamplifiers of the start detector have seen a coincident signal within a time-window of 1.391 ns.—TODO: why this time window?— The overall searching window of the start detector was set to 2  $\mu\text{s}$ , see figure 9. For the MWPC0 which is mounted right at the beam entrance of Cave C no hit multiplicity cuts were applied considering its operating mode, which is designed for charge sharing between the readout pads.

### 3. Projectile's focus on the active target region:

To assure that the incoming  $^{12}\text{C}$  ion hits the target it is necessary to select only events where the projectile is focussed to the active target region. Therefore strict cuts on the MWPC0 x and y position are applied. This was achieved by fitting the x and y distribution of the MWPC0 (without any restrictions on it) by a gaussian function. The selection of focused incoming projectiles was then restricted to events with hits in MWPC0 within the  $\pm 1\sigma$  region in the x and y position, see figure 10 and 11.

The MWPC0 x-position and the available projectile angle in the x-y plane from the R3BMUSIC is used to propagate the corresponding x-position on the target location to further check that the selected projectiles hit the target parallel to the z-position (= beam direction) and do only have a minimal incident angle, see

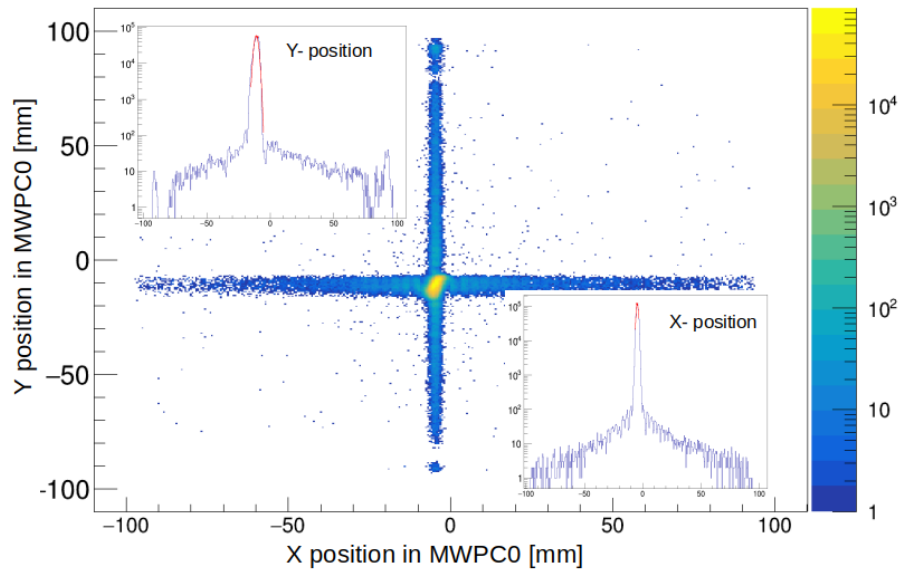


Figure 10: x-y position of incoming ion on MWPC0.

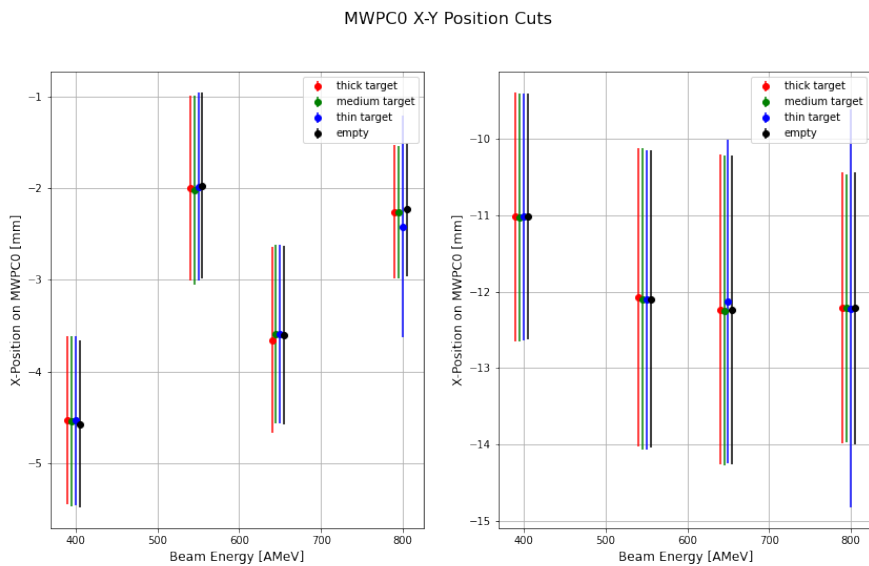


Figure 11: Overview of  $\pm 1\sigma$  cuts in x and y in MWPC0 for empty/target runs. TODO: labelling on the right side is wrong! (should be y!)

figure 12.

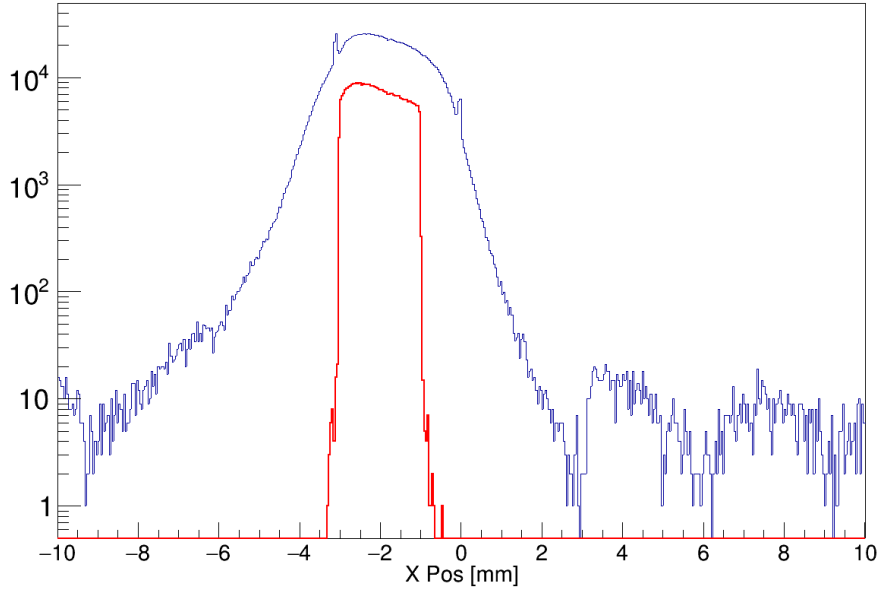


Figure 12: Propagated x-position on target location from measured x-value on MWPC0 and x-y plane angle measurement from R3BMUSIC. The target area is 3 x 3 cm. In red the selected events with  $\pm 1\sigma$  cut in x and y position in MWPC0, in blue all events.  
TODO: which run is this?

### 4.3 Charge Changing Cross Section Measurement

The charge changing cross section refers to a measure of the probability that the incoming projectile will undergo a reaction inside the target that changes its charge. To measure the charge changing cross section it can be referred to formula 8 where in this case  $N_2$  is the number of survived carbon isotopes, i.e. projectiles which did not change their charge state. For this measurement only the data from the double ionisation chamber TWIN Music (see section 3.3.2) needs to be read out and analyzed.

While for the event selection before the target the cut conditions can be arbitrarily strict (it will only have an impact to the statistics and the derived statistical error), cuts on the downstream detectors need to be avoided if at all possible. Too selective cuts on the identification of  $N_2$  can distort the measurement.

#### 4.3.1 TWIN MUSIC Calibration

For the analysis of data in TWIN MUSIC - different to the upstream detectors, where calibrated data with default calibration parameters is used - the so called *mapped* raw

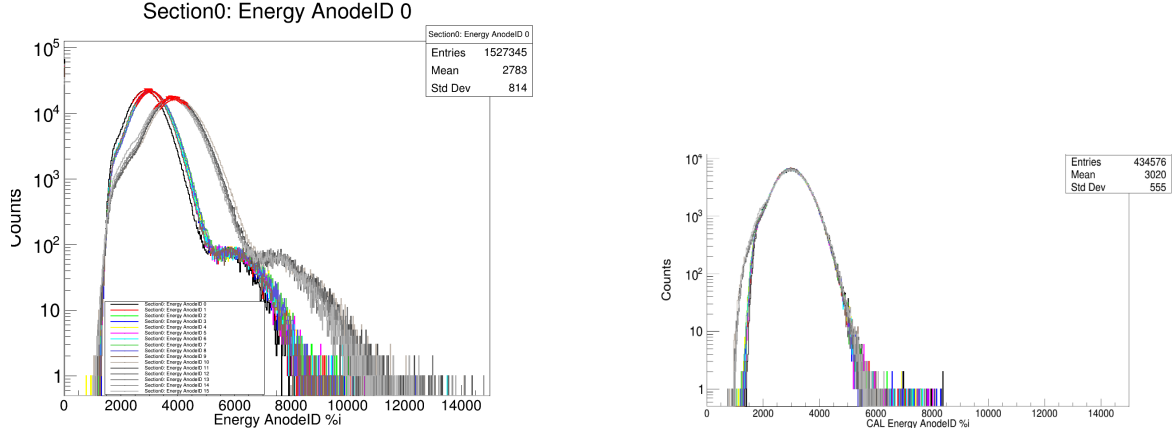
level data is processed. In the mapped level TWIN MUSIC provides following information:

- **SectionID:** The detector is a double ionisation chamber and as such divided into four parts (in beam perspective): section 1 - right down; section 2 - right up; section 3 - left down; section 4 - left up. For the S444 experiment only section 1 was operated and accordingly centered on the beam spot.
- **AnodeID:** TWIN MUSIC has 16 anodes for energy-loss readout and one reference anode (anodeID = 17).
- **Time:** Each hit in each anode gets assigned to a time. Each time has individually no meaning. The drift time (in ns) of the electrons from the ionisation process of the gas by the inflying projectile (or the fragments of it) to the anode is calculated by subtracting the individual anode time by the time of the reference anode. The reference anode receives its clean signal from a constant fraction discriminator of the start detector.
- **Energy:** Each hit in each anode gets assigned to an energy - except the hit in the reference anode. To reconstruct the charge of the crossing through charged particle anodewise or detectorwise the parametrization formula  $Z = [0] + [1]*\sqrt{E} + [2]*E$  is used.

The calibration of the TWIN energy for each anode is done run-wise. For the TWIN MUSIC only events where all anodes having exactly one hit (including the reference anode) are chosen. The most prominent peak ( $Z = 6$ ) was fitted with gaussian function. The calibration was then done by determining the scaling factor for each anode that shifts the mean of the gaussian fits to the same position, see figure 13. For this analysis the peaks were shifted to  $\Delta E = 6$ . Since  $\Delta E \propto Z^2$  holds, the scaled  $\Delta E$  value, even though peaking at 6, is not equate the charge  $Z = 6$ . TODO: describe better the calibration steps!!! this is not good!

#### 4.3.2 TWIN MUSIC Event Selection

As previously stated cuts on the downstream detectors are avoided. However, events which have hits in one or several anodes in TWIN MUSIC but no signal in the reference anode are discarded as a whole neither contributing to  $N_1$  (incoming selected ions) nor to  $N_2$  (unreacted ions). If no reference time from start CFD signal is available it is not possible to measure the drift time in the individual anodes which makes it not possible to distinguish between signal and noise hits for multi-hit anode events in TWIN MUSIC. The number of events affected by this cut is in the region of few tens. This is negligible



(a) Uncalibrated raw  $\Delta E$  distributions for all 16 anodes for the thick target run, 550 AMeV beam energy. The last six anodes have a slightly different electronics amplification chain.

(b) Gaussian fit applied to prominent peak and shifted to same position.

Figure 13: Fitting procedure in TWIN.TODO: nicer labeling!

to the number of incoming ions  $N_1$  and should not have any dependence whether the projectile reacted or not.

### 4.3.3 Carbon Identification

The identification of carbon isotopes in TWIN is done by reconstructing fragments with charge  $Z = 6$  from 2D plots where coincident mean energy losses  $\Delta E$  for different anode combinations are plotted. Since the TWIN MUSIC is multi-hit capable various strategies were developed to deal with multi-hit events, i.e. when having anodes with multiple hits, decide which hit originates from the final state products from the reaction and which from background and noise.

The default strategy is to use the time information of each hit for selection. It has to be remarked that for the S444 experiment the TWIN MUSIC was read out by two independent MDPP modules[25]. The signals from the first reference anode and the first eight upstream anodes were sent to module 1, the ones from the last eight downstream anodes and the second reference anode were forwarded to module 2. For the first eight upstream anodes the drift time is calculated by subtracting the hit time in each anode by the reference time from the first reference anode and for the last eight downstream anodes accordingly the second reference anode was used.

The time based selection algorithm for multi-hit anodes works as follows:

# incoming projectiles $N_1$	400 MeV/nucleon	550 MeV/nucleon	650 MeV/nucleon	800 MeV/nucleon
Empty	574279(*451*)	453729(*34*)	522451(*44*)	395451(*52*)
thin	569503(*422*)	476323(*33*)	538037(*43*)	481459(*36*)
medium	606578(*431*)	451137(*27*)	500688(*40*)	345654(*46*)
thick	655762(*497*)	436457(*30*)	530869(*29*)	479679(*61*)

(a) Number of clean selected incoming  $^{12}\text{C}$  ions. In brackets number of rejected events because of missing tref in TWIN MUSIC. TODO: change the bracket notation, looks like error number!!

# survived carbon isotopes $N_2$	400 MeV/nucleon	550 MeV/nucleon	650 MeV/nucleon	800 MeV/nucleon
Empty	563382(1.898%)	444618(2.008%)	511923(2.015%)	387513(2.007%)
thin	538245(5.489%)	449422(5.648%)	507557(5.665%)	454099(5.683%)
medium	552763(8.872%)	410376(9.035%)	455159(9.093%)	314119(9.123%)
thick	553935(15.528%)	368004(15.684%)	446115(15.965%)	402696(16.049%)

(b) Number of survived carbon isotopes after the target identified via 2D gaussian fit with borders within  $3.5\sigma$  cut. In brackets the percentage of projectiles with a charge state of  $Z < 6$  after the target.

Table 6: Numbers of incoming projectiles  $N_1$  and survived carbon isotopes  $N_2$  for all energy and target runs.

1. Get the mean drift time for the eight upstream anodes( $t_{mean\_up}$ ) and the eight downstream anodes( $t_{mean\_down}$ )<sup>16</sup>. Anodes with multiple hits do not contribute to this calculation.
2. If there are anodes with muliple hits compare the hit time with the accorging mean drift time ( $t_{mean\_up}$  for any of the eight upstream anodes,  $t_{mean\_down}$  for any of the eight downstream anodes). Calculate herefore the absolute difference between mean drift time and each hit time:

$$\Delta t = |\bar{t} - t_{drift}^i|; i = \text{anodeID } (1-16) \text{ with } \bar{t} = \begin{cases} t_{mean\_up} & \text{for } i \leq 8 \\ t_{mean\_down} & \text{for } i \geq 9 \end{cases} \quad (10)$$

3. For each anodes with muliple hits select the hit with lowest drift time differnce to the mean drift time.

---

<sup>16</sup>For the case all eight downstream anodes have multiple hits, set  $t_{mean\_down} = t_{mean\_up}$  and vice versa

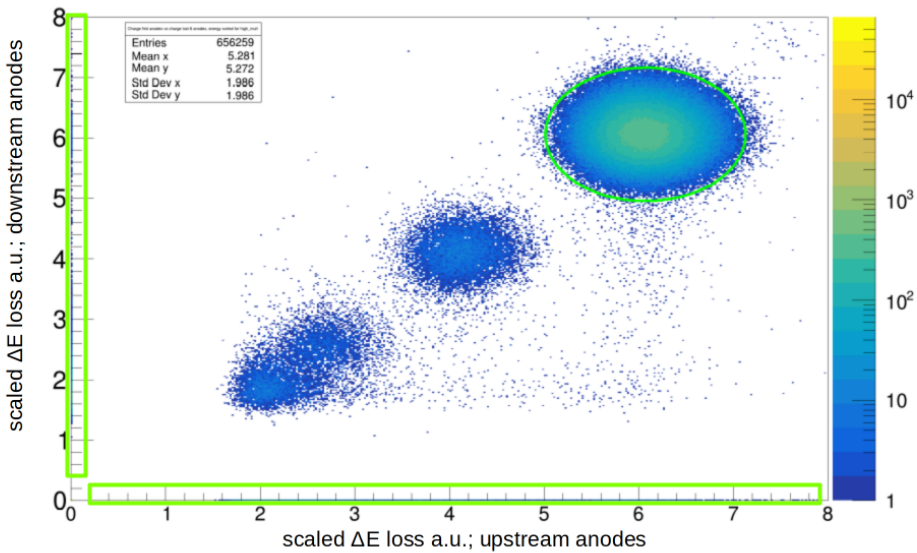


Figure 14: Two dimensional gaussian fit with  $3.5\sigma$  cut on identified carbon isotopes in TWIN MUSIC. The horizontal and vertical side bars contain events where either the eight upstream anodes or downstream anodes have no hit entry. The cluster at scaled  $\Delta E$  loss  $\approx 4.5$  corresponds to boron isotopes ( $Z=5$ ). The clusters for  $Z=4$  (Be) and  $Z=3$  (Li) overlap.

After having selected the appropriate hit for single and multi-hit anodes the mean value for the pre-calibrated  $\Delta E$  loss, see figure 13b, for the eight upstream and accordingly for the eight downstream anodes is determined. Finally, to select the number of survived carbon isotopes the mean  $\Delta E$  of the eight upstream anodes versus the mean  $\Delta E$  of the eight downstream anodes is plotted. To retrieve the number of survived carbon isotopes following two-dimensional gaussian fit is applied on the 2D plot on the charge  $Z = 6$  blob, see figure 14:

$$f(x) = Ae^{-\frac{1}{2}((\frac{x-\bar{x}}{\sigma_x})^2 + (\frac{y-\bar{y}}{\sigma_y})^2)} \quad (11)$$

where  $x$  is the mean rescaled energy loss of the first upstream anodes and  $y$  the according eight downstream anodes. The number of survived carbon isotopes is given by the integral of events within the 2D gaussian fit. Since the anodes were read out by two independent MDPP modules with slightly different thresholds also events along the histogram axes with no hit entry in either the upstream anodes or downstream anodes are analyzed. For those events a one dimensional gaussian cut is applied using the parameters from equation 11 (see horizontal and vertical bars in figure 14).

To get the charge changing cross section values equation 8 has to be applied where both the number of survived carbon isotopes for target run and empty run are determined via the 2D gaussian fit as in figure 14. The number of target particles, are defined by

the target thickness and its density and are listed in section 4.1. The resulting charge

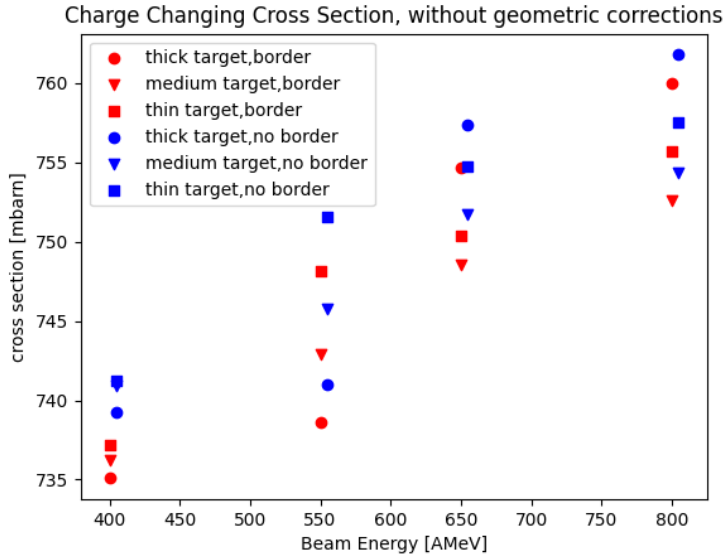


Figure 15: Charge changing cross section without geometry corrections. The red data points result from considering also events with only hits in the upstream or downstream anodes, the blue data points don't take these events in consideration.

changing cross sections are summarized in figure 15 once with consideration of the vertical/horizontal bars in figure 14 and once without. Hits within the  $3.5\sigma$  gaussian fit are identified as carbon isotopes. To get the optimal  $\sigma$  cut on the two dimensional gaussian fit on the energy losses of the upstream anodes versus downstream anodes the charge changing cross section for all targets and all energies was systematically measured for  $\sigma$ -cuts in the range of 1 to 5  $\sigma$ , see figure 16. In the region  $\sim 3.5\sigma$  the variation of the cross section is minimal. Another method to assert the number survived

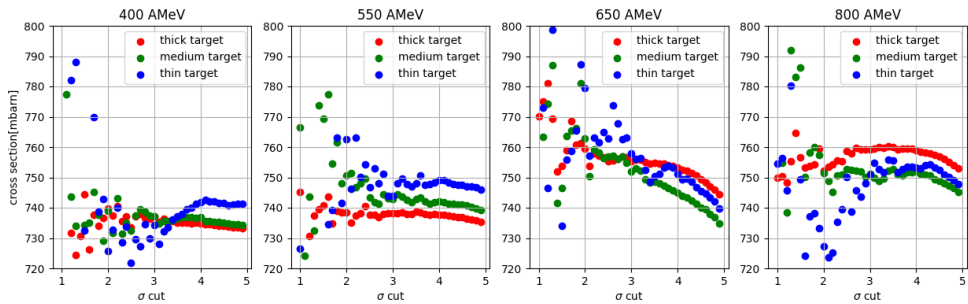


Figure 16: Measured charge changing cross sections according to the  $\sigma$  cut applied on the figure 14 (with borders) for the different target thicknesses and beam energies.

carbon ions is to apply a diagonal cut on the 2D  $\Delta E$  histogram. To set the slope and offset of the diagonal cut line firstly the two dimensional gaussian fit is applied, same

as for the previous method. Then the intersection point between the  $3.5\sigma$  ellipse and the identity line ( $\Delta E$  upstream anodes =  $\Delta E$  downstream anodes) is found. Through this point, perpendicular to the identity line, the diagonal line is drawn. Everything above the diagonal line is considered as survived carbon ions. Moreover the borders are considered within the  $3.5\sigma$  cut, see figure 17. The effects of the two different methods

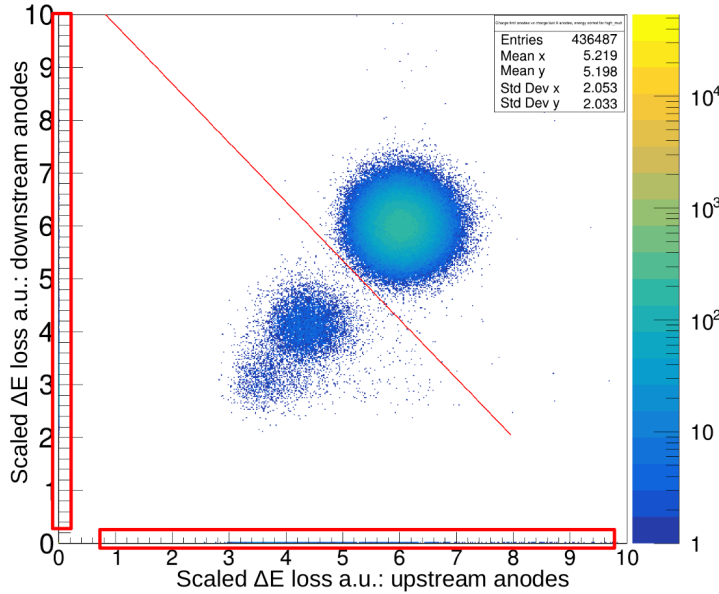


Figure 17: Diagonal cut on identified carbon isotopes along the gaussian  $3.5\sigma$  cut with borders. All hits above the diagonal line are counted as carbon isotopes. Histogram from thick target run, 550 AMeV beam energy.

used for the identification of the carbon isotopes for the charge changing cross section is summarized in figure 18. The differences in the measured cross sections are within the margin of error herefore both methods are comparable, as expected. To check wether single anodes or groups of anodes are malfunctioning the charge changing cross section measurement was repeated using only certain anodes for the charge identification:

- a) anodes 2-8 versus anodes 9-15 (omitting first and last anode)
- b) anodes 1-4 versus anodes 5-8 (upstream anodes)
- c) anodes 5-8 versus anodes 9-12 (central anodes)
- d) anodes 9-12 versus anodes 13-16 (downstream anodes)

The results from the measurement are summarized in figure 19. The difference between the default gaussian fit method (with  $3.5\sigma$  cut and considering the borders) considering all 16 anodes and applying the same method but omitting the first and last anode is minimal over all four beam energies. When selecting only 8 out of 16 anodes instead the

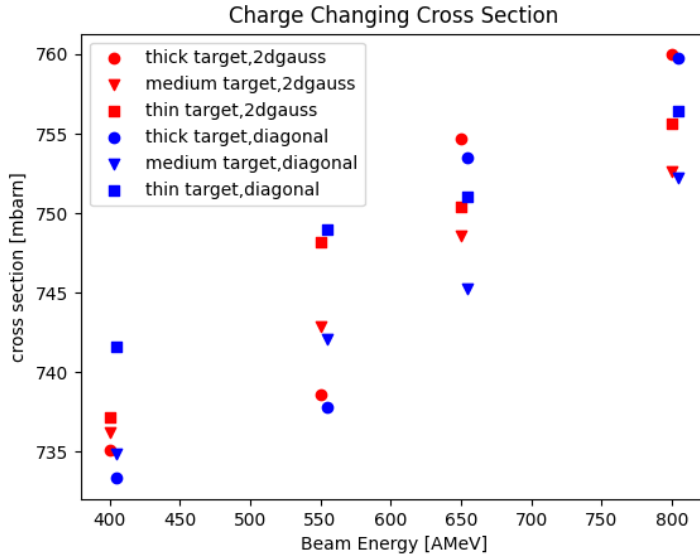


Figure 18: Comparison of charge changing cross section measured via 2D gaussian fit cut and diagonal cut. The differences are within the margin of error.

cross sections are systematically lower when going to high beam energies. The energy loss inside the TWIN MUSIC decreases with higher beam intensities, according to the Bethe-Bloch formula:

$$-\frac{dE}{dx} = K z^2 \frac{Z}{A} \frac{1}{\beta^2} \left( \frac{1}{2} \ln \frac{2m_e c^2 \beta^2 \gamma^2 T_{\max}}{I^2} - \beta^2 - \frac{\delta(\beta\gamma)}{2} \right) \quad (12)$$

where:

$$K = 4\pi N_A r_e^2 m_e c^2 \approx 0.307 \text{ MeV cm}^2 \text{ g}^{-1},$$

$z$  = charge of the incident particle (in elementary charge units),

$Z$  = atomic number of the target material,

$A$  = atomic mass of the target material,

$\beta = \frac{v}{c}$  = velocity of the particle relative to the speed of light,

$\gamma = \frac{1}{\sqrt{1 - \beta^2}}$  = Lorentz factor,

$T_{\max}$  = maximum kinetic energy transferable to an electron in one collision,

$I$  = mean excitation potential of the target material,

$\delta(\beta\gamma)$  = density effect correction.

The behaviour of  $dE/dx$  for small  $\beta$ - values are dominated by the  $1/\beta^2$  term. The decrease of deposited energy for larger beam energies has as consequence a lower relative resolution in the two dimensional  $\Delta E$  loss histogram (see figure 14) reflecting the

poissonian distribution properties. In addition reducing the number of readout anodes by a factor two degrades the resolution by a factor  $\sqrt{2}$ <sup>17</sup>. This has as consequence that the ellipsis with  $3.5\sigma$  cut incorporates a non negligible amount of boron isotopes which are counted as survived carbon isotopes which in turn reduces the measured charge chaning cross section.

While in the above measurements a time based secelction algorithm for multi-hit an-

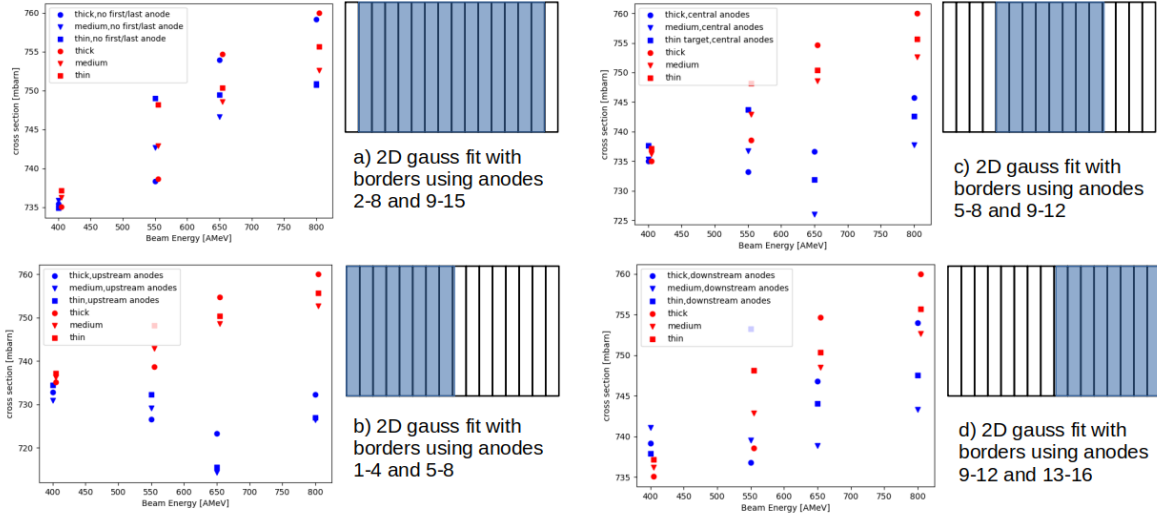


Figure 19: Measurement of charge changing cross sections using different anode sections to make the two dimensional gaussian fit on the identified carbon isotopes. Red: using all 16 anodes. Blue: the various combinations.

odes was used also an energy based selection was tested. This algorithm selects for multi-hit anodes the hit with the highest energy as physical hit and discards all others, as they are considered as background/noise. Figure 20 compares the time based method versus the energy based method. In both cases a two dimensional gaussian  $3.5\sigma$  cut is applied as in figure 14 and the borders are counted as well. The difference in the outcome is negligible. This can be explained since noise or background signal should be both uncorrelated to the event time and at a low energy level and are therefore filtered by both algorithms. The final charge changing cross section measurements with 2D gaussian fit applying a  $3.5 \sigma$  cut and including the borders of the histogram are summarized in figure 21. At this stage also the statistical errors are incorporated.

<sup>17</sup>It can be assumed a similar  $\Delta E$  distribution for all anodes. Hence the central limit theorem can be applied where  $\sigma = \frac{\sigma_{anode}}{\sqrt{n}}$  with  $n = \text{number of anodes}$ .

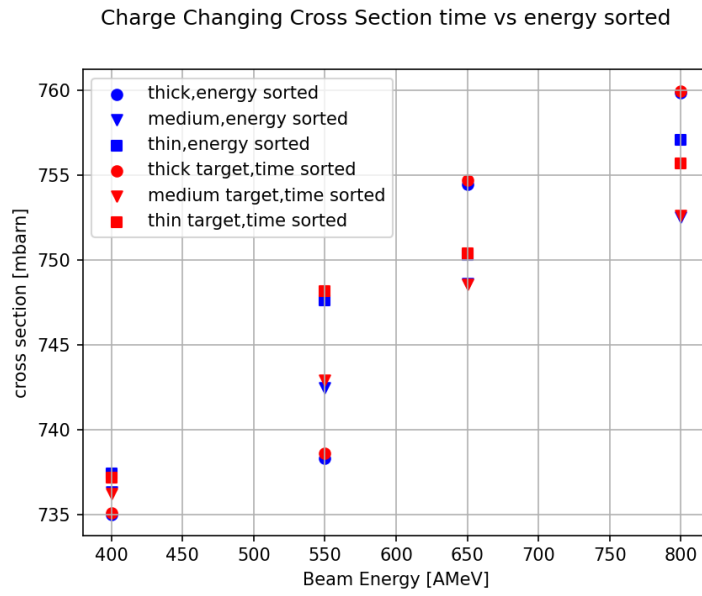


Figure 20: Comparison of charge changing cross section measurements when using time sorting algorithm(red) and energy sorting algorithm(blue) for multi-hit anodes.

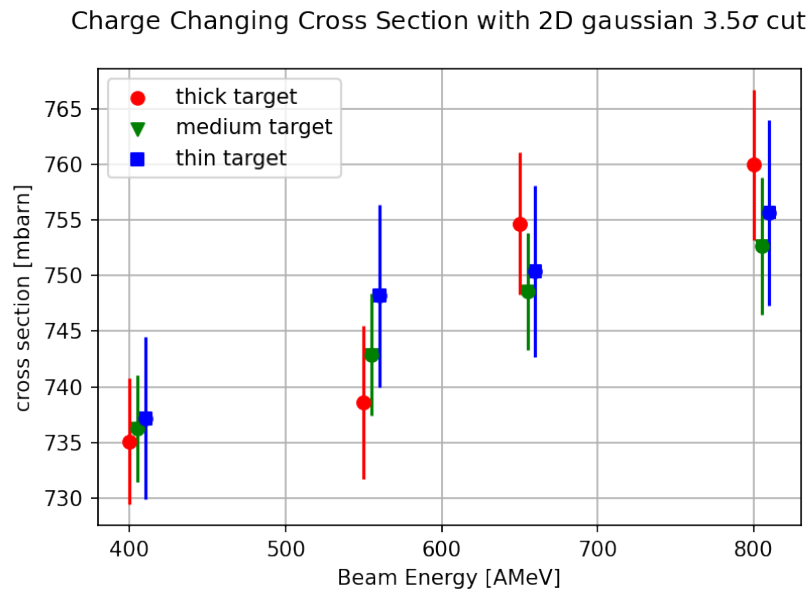


Figure 21: Measurement of charge changing cross sections using all 16 anodes of the TWIN MUSIC applying the 2D gaussian fit and considering the borders as in figure 14.

## 4.4 Geometric Corrections

For the S444 experiment only section 1 (right down) of the TWIN MUSIC, which was centered on the beam spot, was operated. As consequence full geometric efficiency could not be assumed. To visualize the restricted geometric efficiency of the TWIN MUSIC the position in x and y (perpendicular plane to the beam direction) on the MWPC1 in front of the ionisation chamber was plotted, once without any conditions on the TWIN MUSIC and once with the condition of having identified a carbon isotope (with the 2D gauss-fit method as described in chapter 4.3.3), see figure 22. The large active surface area of  $200 \times 200 \text{ mm}^2$  of the MWPC1 affirms that all the carbon fragments are detected<sup>18</sup> whereas the TWIN MUSIC behind it, with an active surface of  $55 \times 110 \text{ mm}^2$  (section 1), is not sensitive to the scattered fragments with large deflection angle.

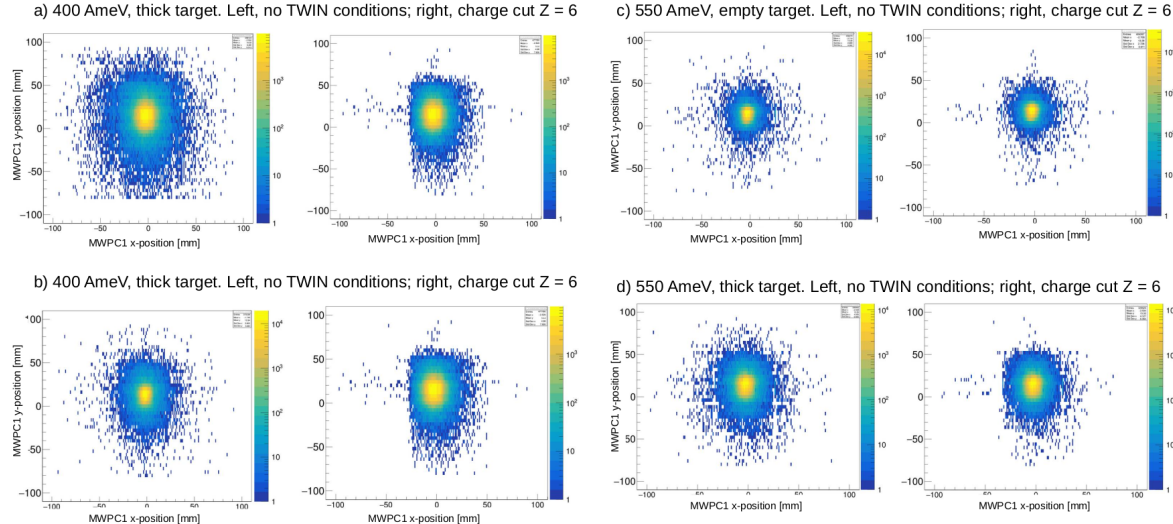


Figure 22: Distribution in x and y on MWPC1 for different energies with and without target. TODO: subplot b) wrong naming,it's the empty run 400 AMeV.

The efficiency loss depends on the target thickness - for thicker targets the geometric distribution of the fragments is broader and therefore the efficiency loss larger - and the beam energies - for larger beam energies the scattering angles decrease due to the boost effects, the efficiency loss gets smaller. This means, that the efficiency loss needs to be compensated runwise. These efficiency effects can be observed in figure 22.

To compensate correctly for the geometric efficiency it has to be considered that for the charge changing cross section measurement only the carbon isotopes after the target are counted in the TWIN MUSIC. Therefore the correction should only be applied to

<sup>18</sup>This statement does not hold for light fragments as protons or deuterons. Their deflection angle exceeds the geometric acceptance of the MWPC1.

the carbon isotopes ( $Z = 6$ ) on the x-y distribution on the MWPC1, see figure 22. The geometric efficiency correction is done graphically on the x-y distribution of the MWPC1 for carbon isotopes by following procedure:

### 1. Correction for the x-position distribution:

- (a) First fit x-distribution with double-gaussian function with five free parameters and common mean value  $\mu_x$

$$f(x) = A \cdot \exp\left(-\frac{(x - \mu_x)^2}{a^2}\right) + B \cdot \exp\left(-\frac{(x - \mu_x)^2}{b^2}\right) \quad (13)$$

- (b) Fit again within range  $\mu_x \pm \epsilon_x$ . The parameter  $\epsilon_x$  is fixed by educated guess, TODO. As  $\mu_x$  take the value from the fit in the previous step. A fit for the central region of the x-distribution is obtained,

$$f(x)_{central}(A_{central}, a_{central}, B_{central}, b_{central}, \mu_{central}).$$

- (c) The obtained fit function  $f(x)_{central}$  is then used to compare with the data distribution( $f(x)_{data}$ ) in the border regions  $[-100, \mu_{central} - \epsilon_x]$  and  $[\mu_{central} + \epsilon_x, 100]$ . Since only the left border region (low x-positions) is affected by the limited geometric acceptance, the right border region can be used for correction:

$$\Delta_{xcorr} = \int_{\mu_{central} + \epsilon_x}^{100} f(x)_{data} - f(x)_{central} - \int_{-100}^{\mu_{central} - \epsilon_x} f(x)_{data} - f(x)_{central} \quad (14)$$

### 2. Correction for the y-position distribution:

- (a) First fit y-distribution with double-gaussian function with five free parameters and common mean value  $\mu_y$

$$f(y)_{fit} = C \cdot \exp\left(-\frac{(y - \mu_y)^2}{c^2}\right) + D \cdot \exp\left(-\frac{(y - \mu_y)^2}{d^2}\right) \quad (15)$$

- (b) The obtained fit function  $f(y)$  is then used to compare the data distribution( $f(y)_{data}$ ) in the border regions  $[-100, \mu_y - \epsilon_y]$  and  $[\mu_y + \epsilon_y, 100]$ . The parameter  $\epsilon_y$  is fixed by educated guess, TODO. As  $\mu_y$  take the value from the fit in the previous step. Same as for the x-correction both border regions are compared. The high border region (high y-positions) affected by the limited geometric acceptance while the low border region (low y-positions) has full geometric acceptance.

$$\Delta_{ycorr} = \int_{-100}^{\mu_{central} - \epsilon_y} f(y)_{data} - f(y)_{fit} - \int_{\mu_y + \epsilon_y}^{100} f(y)_{data} - f(y)_{fit} \quad (16)$$

3. To correct the number of survived carbon isotopes  $N_2 = N_{carbon}$  both corrections in x and y are applied<sup>19</sup>

$$N_2^{corr} = N_2 + \frac{\Delta_{xcorr} + \Delta_{ycorr}}{N_2} \quad (17)$$

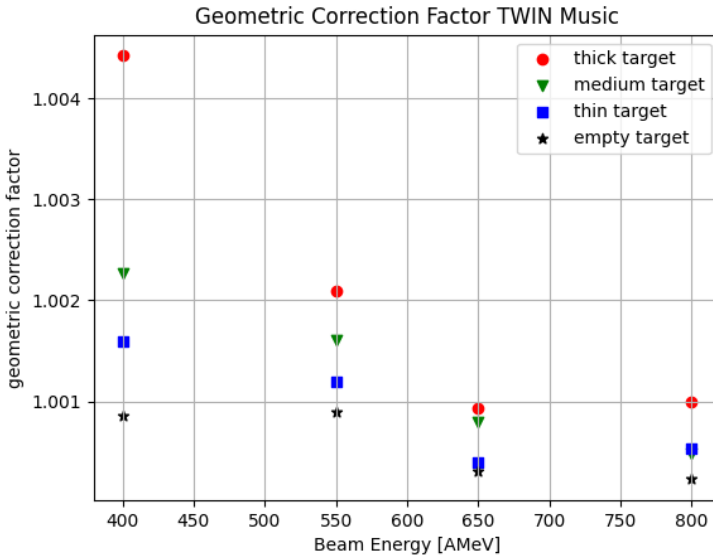


Figure 23: Geometric correction factors from limited geometric efficiency of TWIN Music.

Figure 23 summarizes the geometric correction factors  $\epsilon_{geo\_corr}$  obtained from the graphical reconstruction of missed TWIN Music events as described above. The correction factor is subsequently applied to the charge-changing cross-section, resulting in the final corrected charge-changing cross-section:

$$\sigma_{geo\_corr} = -\frac{1}{N_t} \ln\left(\frac{N_1^E}{N_2^E} \frac{N_2}{N_1} \cdot \epsilon_{geo\_corr}\right) = -\frac{1}{N_t} \left( \ln\left(\frac{N_1^E}{N_2^E} \frac{N_2}{N_1}\right) + \ln(\epsilon_{geo\_corr}) \right) \quad (18)$$

Figure 24 shows the measured charge changing cross section once without considering the the limited geometric acceptance of the TWIM Music and once applying the geometric correction factors as presented in equation 18. As expected significantly affected by the geometric correction are runs with 400 and 550 AMeV beam energy whereas at beam energies of 650 and 800 AMeV the effect is exceptionally small since at high beam energies the fragments after the target preceive a strong boost effect in beam direction which constrains the distribution in the x-y-plane.

---

<sup>19</sup>Under the assumption that x and y are uncorrelated where the x-y distribution on the MWPC1 is given by  $f(x, y) = f(x) \cdot f(y)$ .

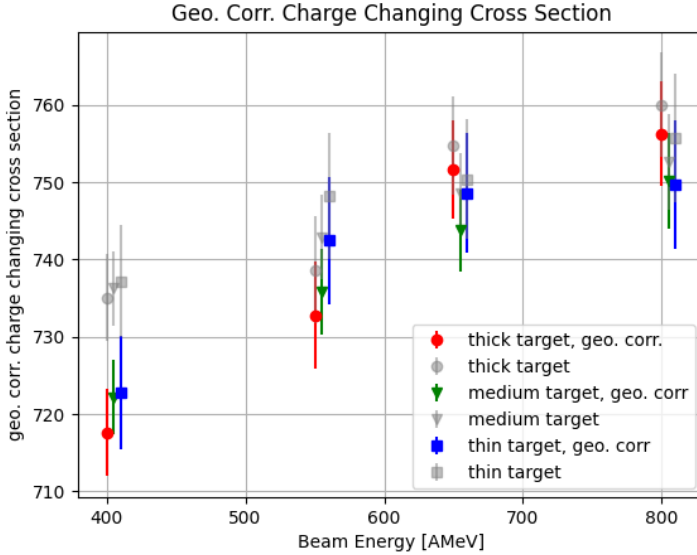


Figure 24: Charge changing cross section with applied geometry corrections. In gray: charge changing cross section measurements before applying corrections, as in figure 19.

## 4.5 Isotope Correction - Total Interaction Cross Section

The general formulation for the calculation of cross sections in equation 8 can be used to determine the cross section for specific channels depending on the definition of  $N_2$ . In the previous subsection 4.3 where the charge changing cross section was measured,  $N_2$  had to be sensitive to the charge of the outgoing fragment. Therefore  $N_2$  was defined as the number of survived carbon isotopes, i.e.  $N_2 = N_2^{Z=6}$ . For the measurement of the total interaction cross section  $N_2$  has to be sensitive to both proton and neutron number of the fragments.  $N_2$  is herefore restricted to the number of survived  $^{12}\text{C}$  isotopes, i.e.  $N_2 = N_2^{^{12}\text{C}}$ . Since  $N_2^{^{12}\text{C}}$  is a subset of  $N_2^{Z=6}$ ,  $N_2^{^{12}\text{C}}$  can be determined by identifying and disentangling the number of survived  $^{12}\text{C}$  isotopes from the set of events with carbon isotopes  $N_2^{Z=6}$ . For that reason the positional correlations on the x-coordinate of MWPC2 (upstream to GLAD) and the MWPC3 (downstream to GLAD) are exploited. The GLAD magnet, which acts as a mass spectrometer, deflects the passing through fragment. Depending on its proton to neutron ratio the fragment is deflected more or less, described by the formula for magnetic rigidity:

$$B \cdot \rho = \frac{\gamma \cdot m \cdot v}{q} \quad (19)$$

where:

- $B$  is the strength of the magnetic field,
- $\rho$  is the radius of curvature of the particle's trajectory,
- $\gamma$  is the Lorentz factor,
- $v$  is the velocity of the particle,
- $m$  is its mass,
- $q$  is its charge.

Figure 26 shows the x distribution on MWPC2 versus MWPC3 for the thick target run at a beam energy of 400 AMeV. The main diagonal line corresponds to the  $^{12}\text{C}$  isotopes. From all isotopes they have the largest mass to proton ratio ( $n+p/p$ ) and are therefore less deflected by the magnetic field of GLAD. The less prominent line below corresponds to  $^{11}\text{C}$  isotopes and on the lower edge few events with  $^{10}\text{C}$  are visible. To identify the number of survived  $^{12}\text{C}$  fragments a graphical selection of the  $^{12}\text{C}$  isotopes - the main diagonal line - is applied.

#### Graphical Selection Algorithm:

- Fit the main diagonal line, which corresponds to the  $^{12}\text{C}$  isotopes, with a linear fit function  $f(x_{mw2}) = a \cdot x_{mw2} + b$ .
- To get the most accurate intersection line between  $^{12}\text{C}$  isotopes and all lighter carbon isotopes the linear fit function from the previous step is taken as starting point. Iteratively the offset value  $b$  is reduced by  $b_i = b_{i-1} - 1$ . For all iteration steps the ratio  $r_{^{12}\text{C}(i)}$  of hits below the linear fit function and the total number of hits in the histogram is calculated.
- The derivative  $\frac{dr_{^{12}\text{C}}(i)}{db_i}$  is calculated.
- Finally the offset  $b_i$  with the largest value for  $\frac{dr_{^{12}\text{C}}(i)}{db_i}$  is selected as cutting line between  $^{12}\text{C}$  isotopes and  $^{11}\text{C}/^{10}\text{C}$  isotopes<sup>20</sup>.

The ratio  $r_{^{12}\text{C}}$  is unaffected by detector efficiencies of MWPC2 and MWPC3<sup>21</sup> and therefore the ratio  $r_{^{12}\text{C}}$  can be applied directly as isotope correction to calculate the total interaction cross section:

$$\sigma_I = \sigma_{geo\_corr} + \sigma_{iso}$$

With the isotope correction cross section  $\sigma_{iso}$ :

$$\sigma_{iso} = -\frac{1}{N_t} \ln(r_{^{12}\text{C}})$$

---

<sup>20</sup>For empty target runs the offset  $b$  is manually selected

<sup>21</sup>Under the assumption of constant efficiency over  $x_{mw2}$  and  $x_{mw3}$

To calculate the isotope correction cross section six different methods were employed and compared with each other:

- **MWPC2 and MWPC3 hit-level data:**

For all MWPCs the standard *cal-to-hit* step sorts the calibrated hits in the detector according to the calibrated charge deposited in the pads. The final position (in mm) is determined by selecting the hit with the highest charge deposition  $Q_{max}$  and its left ( $Q_L$ ) and right neighbour ( $Q_R$ ) pads<sup>22</sup>. These charge and position values are inserted in the "hyperbolic squared secant" function [26] with the following charge distribution function:

$$Q(x) = \frac{a_1}{\cosh^2\left(\frac{\pi(x-a_2)}{a_3}\right)}$$

where  $a_1$  is the amplitude of the distribution  $Q_{max}$ ,  $a_2$  its centroid, and  $a_3$  derives as follows:

$$a_3 = \frac{\pi\omega}{\cosh^{-1}\left(0.5 \times \left(\sqrt{\frac{Q_{max}}{Q_L}} + \sqrt{\frac{Q_{max}}{Q_R}}\right)\right)}$$

$\omega$  being the width of the pads. The centroid of the distribution, which is used as final hit position in the *hit-data* level, can be deduced from:

$$a_2 = \frac{a_3}{\pi} \times \tanh^{-1}\left(\frac{\sqrt{\frac{Q_{max}}{Q_L}} - \sqrt{\frac{Q_{max}}{Q_R}}}{2 \sinh\left(\frac{\pi\omega}{a_3}\right)}\right)$$

Figure 25 shows the "hyperbolic squared secant" function with the inserted values for  $Q_{max}$ ,  $Q_R$  and  $Q_L$ . The "hyperbolic squared secant" function is used to determine the x hit position as well as the y hit position for all MWPCs. Figure 26 shows the  $x_{mw2}$  versus  $x_{mw3}$  distribution of carbon isotopes for the 400 AMeV run with the thick target. The two correlated lines corresponding to the  $^{12}\text{C}$  and  $^{11}\text{C}$  isotopes can clearly be distinguished. The vertical line can be interpreted as amount of events where the incoming centered carbon fragment gets scattered by air or the detector material in place between MWPC2 and MWPC3. The horizontal wide spread line has no physical interpretation and can rather be explained by the *cal-to-hit* step in MWPC2: For events where there is not a spatially constrained hit cluster but sparse hits the hyperbolic squared secant function may pick the wrong  $Q_{max}$  and therefore wrongly reconstructs the x position in MWPC2.

- **MWPC2 and MWPC3 data with own "hit-clustering" level:**

To overcome the issue with potentially wrong x-position reconstruction in the

---

<sup>22</sup>In case no charge deposition in one or both neighbours the charge value is set to 1 respectively.

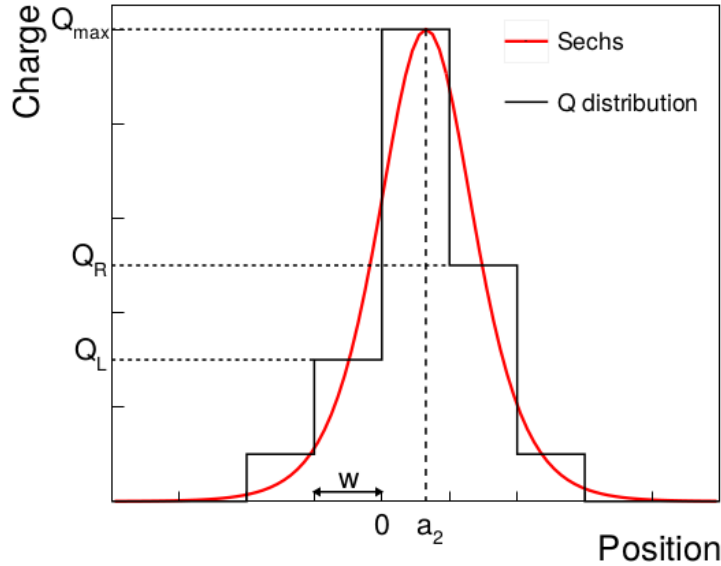


Figure 25: Figure taken from [6], with  $w$  being the width of the cathode pads of the MWPC and  $a_2$  the final position value of the hit determined by the hyperbolic squared secant function (in red). In black the measured charge deposition distribution in the MWPC.

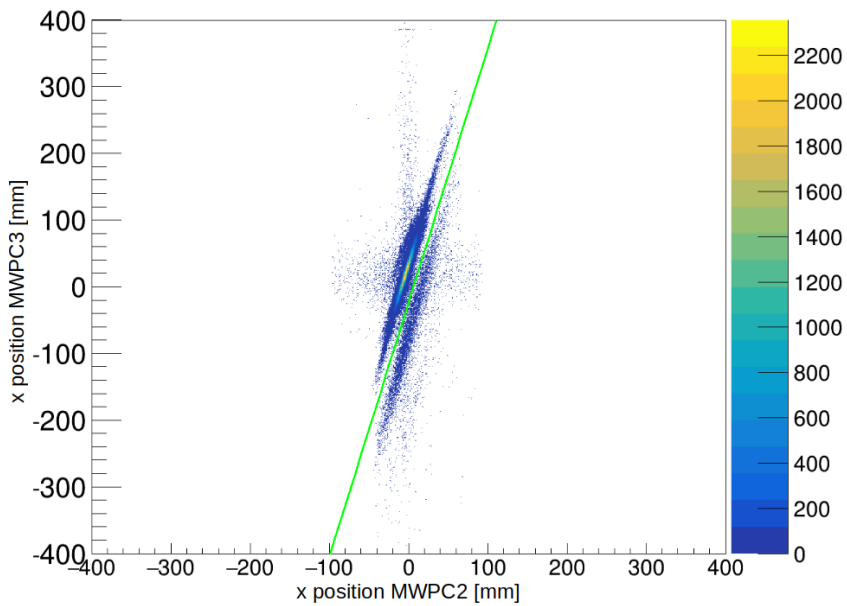
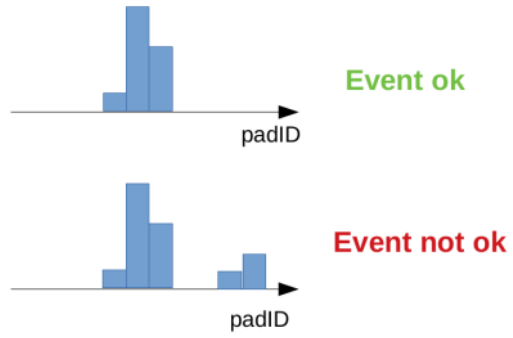


Figure 26: Distribution of  $x$  in MWPC2 and MWPC3 for the 400 AMeV run with thick target. The green line corresponds to the intersection line between  $^{12}\text{C}$  and  $^{11}\text{C}/^{10}\text{C}$  isotopes fixed on the graphical selection algorithm.

Figure 27: Restricted event selection for MWPC2 and MWPC3: only events with one single coherent (i.e. without any holes) cluster are accepted.



MWPCs the event selection on MWPC2 and MWPC3 was restricted to events where both MWPC2 and MWPC3 have only one spatially constrained cluster (see figure 27) to avoid ambiguities in the position determination. This method strongly retains uncorrelated hits in MWPC2 and MWPC3.

Figure 28 shows the distribution of  $x$  in MWPC2 and MWPC3 using the own hit-clustering reconstruction. This reconstruction method removes the uncorrelated horizontal line which was observed in figure 26. However the statistics are reduced by  $\approx 35\%$ <sup>23</sup>.

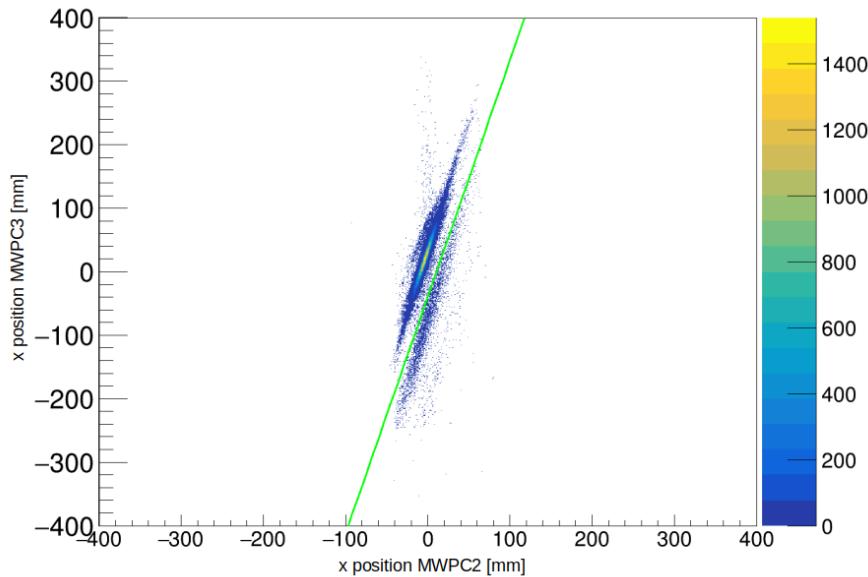


Figure 28: Distribution of  $x$  in MWPC2 and MWPC3 using the own hit clustering reconstruction. Thick target run, beam energy 400 AMeV. The green line corresponds to the intersection line between  $^{12}\text{C}$  and  $^{11}\text{C}/^{10}\text{C}$  isotopes fixed on the graphical selection algorithm.

---

<sup>23</sup>Number of entries in the 2D plot for default reconstruction method: 533816, for the own hit clustering reconstruction: 346315 for the 400 AMeV run with thick target.

- **MWPC1 and MWPC3 hit-level data:**

To get the ratio  $r_{^{12}C}$  it is necessary to correlate the x positon before and after the GLAD magnet. This task can be completed by MWPC3 with respect to MWPC2 or MWPC1. Since the MWPC1 is upstream to MWPC2 the positional distribution of the carbon fragments narrower which as consequence makes it more difficult to disentangle  $^{12}C$  and  $^{11}C/^{10}C$  isotopes, see figure 29. Moreover MWPC1 had two noisy pads which distorts the distribution when using the standard *cal-to-hit* step to get the position value, see figure 29.

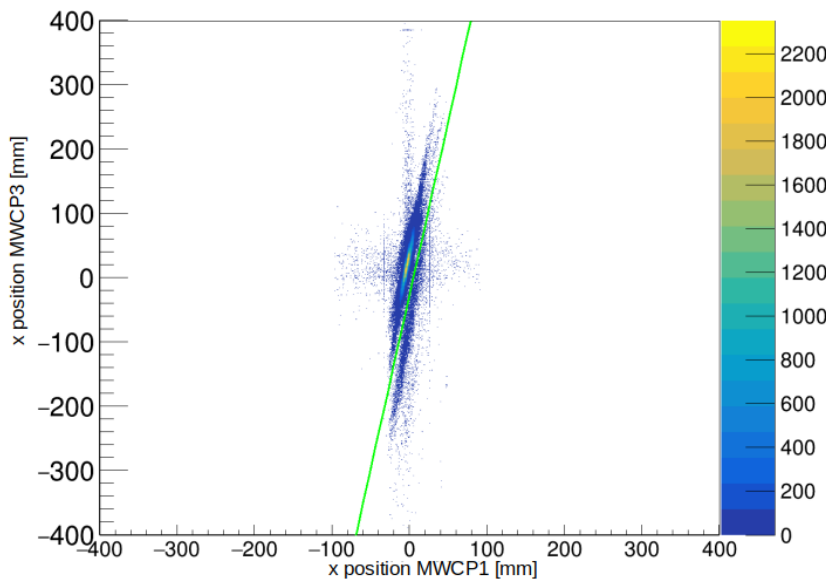


Figure 29: Distribution of x in MWPC1 and MWPC3. Thick target run, beam energy 400 AMeV. The two vertical lines stem from two noisy pads in MWPC1.

- **MWPC1 and MWPC3 data with own "hit-clustering" level:**

Again, to overcome the issue with potentially wrong x-position reconstruction in the MWPCs the own hit clustering reconstruction method, as described above, was applied to MWPC1 and MWPC3 resulting in the 2D plot 30.

- **MWPC2 and MWPC3 with own clustering, quadrant selection in MWPC2:<sup>24</sup>**

The limited geometric acceptance of TWIN MUSIC, described in section 4.4, affects the isotope correction too. The x distribution on the MWPC1/2/3 is cut off on the lower end and the y distribution on the higher end, see figure 22. The  $^{11}C/^{10}C$  isotopes are expected to have a broader x and y distribution. Missing the lower and higher edges in the x and y distribution respectively distorts the  $r_{^{12}C}$  ratio towards higher values. This results in a lower cross section contribution

---

<sup>24</sup>I did the quadrant selection also in MWPC2, outcome really similar, TODO: add to appendix...

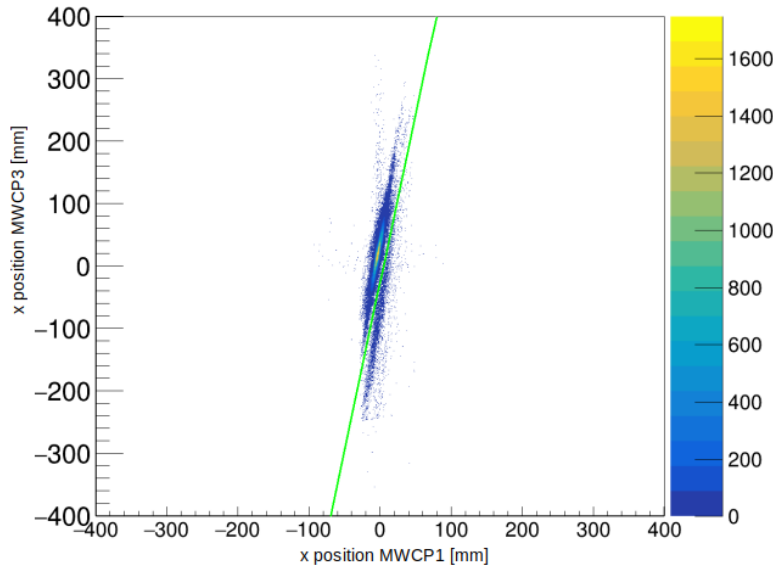


Figure 30: Distribution of x in MWPC1 and MWPC3 using the own hit clustering reconstruction. Thick target run, beam energy 400 AMeV.

of the isotope correction, especially for the low energy runs. To correct for this the x-y distribution in MWPC1 was split into four quadrants, see figure 31. The intersection lines were derived by the mean of the gaussian fit of the x and y distribution. The cross section contribution of the isotope correction was measured for all four quadrants.

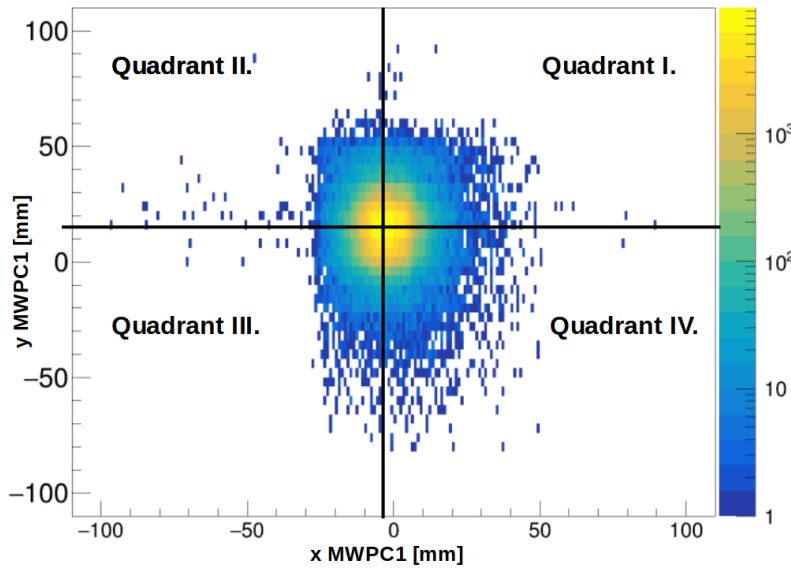


Figure 31: Distribution of x and y in MWPC1 split up in four quadrants. Thick target run, beam energy 400 AMeV.

#### 4.5.1 Results for Isotope Correction Methods

- MWPC2 and MWPC3 hit-level data:

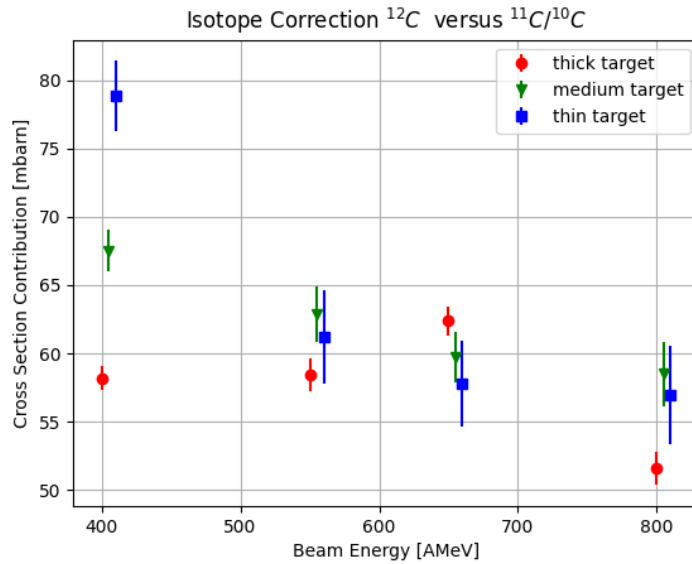


Figure 32: Isotope correction contribution to the total interaction cross section using standard hit level data in MWPC2 and MWPC3.

- MWPC2 and MWPC3 data with own "hit-clustering" level:

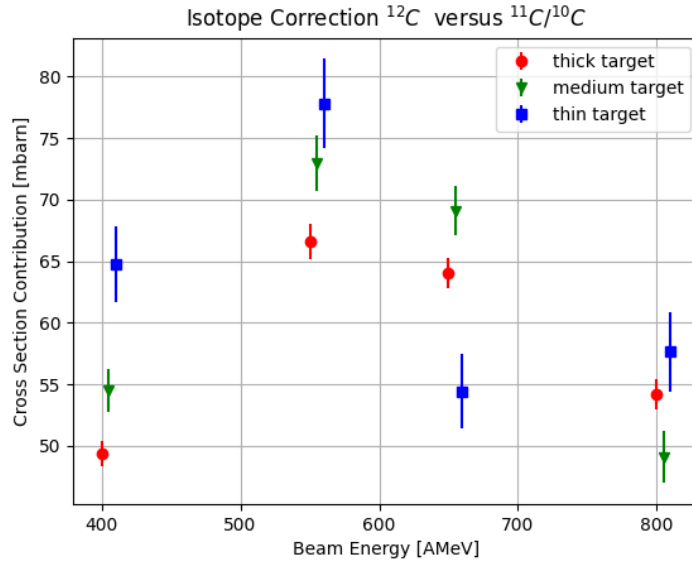


Figure 33: Isotope correction contribution to the total interaction cross section using own hit clustering in MWPC2 and MWPC3.

- MWPC1 and MWPC3 hit-level data:

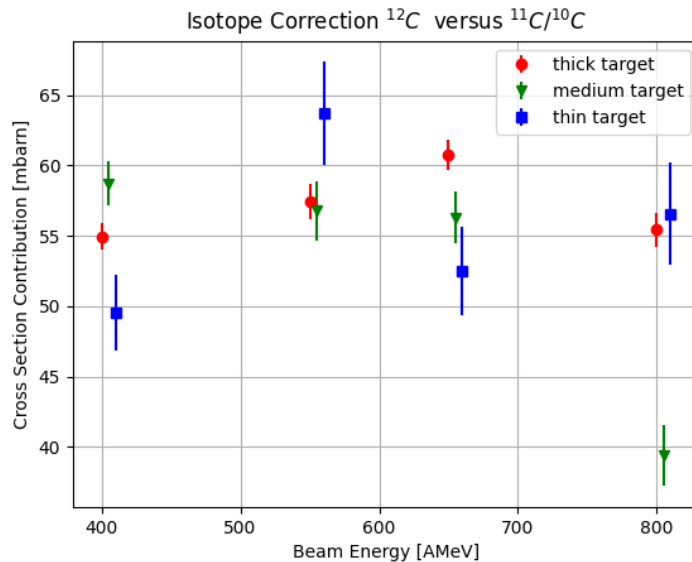


Figure 34: Isotope correction contribution to the total interaction cross section using standard hit level data in MWPC1 and MWPC3.

- MWPC1 and MWPC3 data with own "hit-clustering" level:

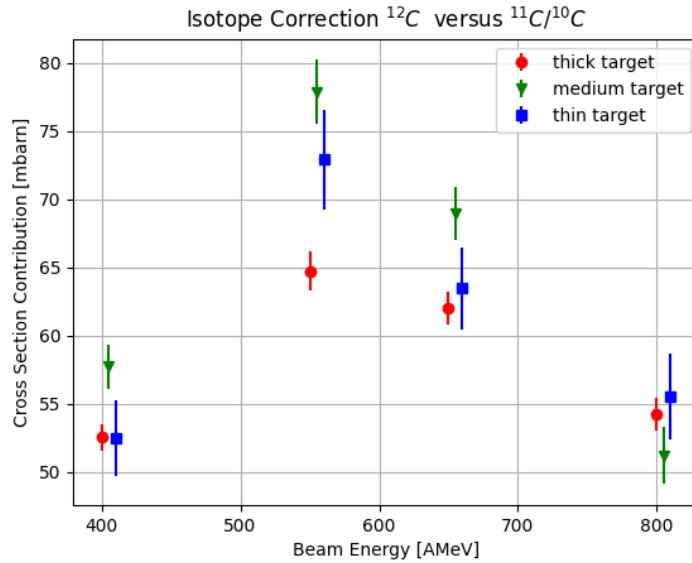


Figure 35: Isotope correction contribution to the total interaction cross section using own hit clustering in MWPC1 and MWPC3.

- MWPC2 and MWPC3 with own clustering, quadrant selection in MWPC1:

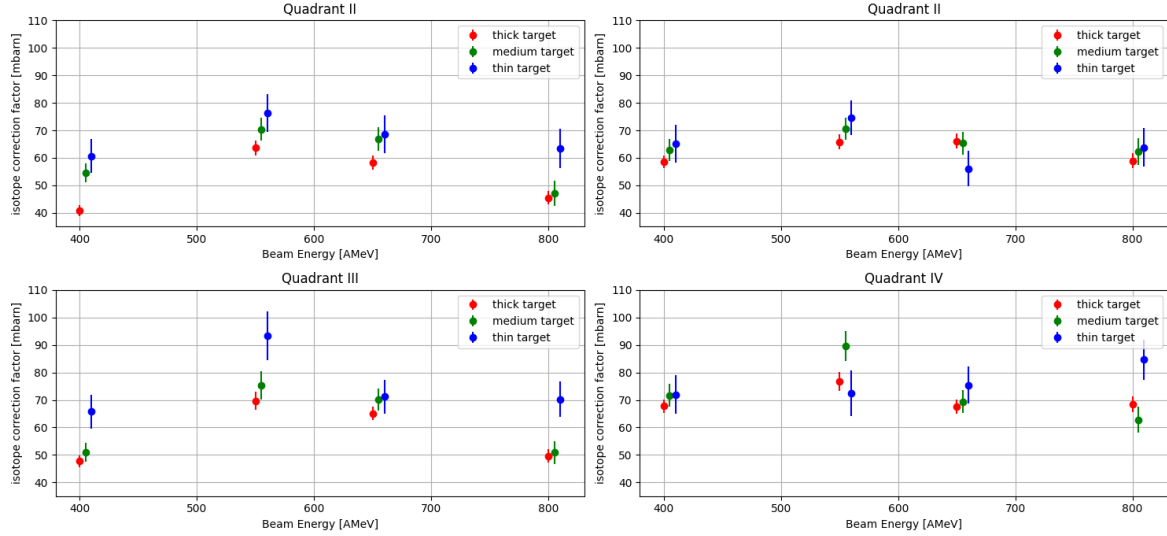


Figure 36: Isotope correction contribution to the total interaction cross section using own hit clustering in MWPC2 and MWPC3. Comparison for different quadrant selection in MWPC1. Quadrant four is the preferred one as it is not affected by limited geometric acceptance of TWIN MUSIC.

## 4.6 Statistical and Systematic Error Analysis

All three measurements presented in this section, the charge changing cross section, the isotopic cross section correction cross section and the total interaction cross section, rely on the transmission method and the error analysis of those measurements are treated the same accordingly. The generic formula for all three measurements was presented in section 4.1, equation 7.

Since all quantities in equation 7 are mutually independent, the gaussian error propagation for statistical and systematical uncertainties is given by:

$$\Delta_{stat./syst.} = \sqrt{\sum_{i=1}^n \left( \frac{\partial f}{\partial x_i} \cdot \Delta_{x_i} \right)^2} \quad (20)$$

with:

$f(x_1, x_2, \dots, x_n)$  the error prone cross section function,

$x_i$  the independent variables ( $N_1, N_2, N_t$ ; see equation 7),

$\Delta_{x_i}$  stat./syst. uncertainties associated to independent variable  $x_i$

#### 4.6.1 Statistical Uncertainties

For the charge changing cross section the combined statistical error is:

$$\Delta\sigma_{\text{stat.}|cc} = \sqrt{\left(\frac{\partial\sigma_{cc}}{\partial N_t}\Delta N_t\right)^2 + \left(\frac{\partial\sigma_{cc}}{\partial P_{\text{surv}|cc}}\Delta P_{\text{surv}|cc}\right)^2 + \left(\frac{\partial\sigma_{cc}}{\partial P_{\text{surv}|cc}^E}\Delta P_{\text{surv}|cc}^E\right)^2} \quad (21)$$

where  $\Delta N_t$  accounts for the uncertainty in the measurement of the target thickness.  $P_{\text{surv}|cc}$ , the surviving probability of having a carbon isotpe in the final state, follows a binomial distribution with  $N_1$  independent experiments and a boolean valued reaction output (survived vs. non-survived). Therefore  $P_{\text{surv}|cc}$  follows the standard error of binomial distributed variable:

$$\Delta P_{\text{surv}|cc}^{(E)} = \sqrt{\frac{P_{\text{surv}|cc}^{(E)} \cdot (1 - P_{\text{surv}|cc}^{(E)})}{N_1^{(E)}}} \quad (22)$$

Inserting in equation 21 gives:

$$\Delta\sigma_{\text{stat.}|cc} = \sqrt{\left(\frac{\sigma_{cc}\Delta N_t}{N_t}\right)^2 + \frac{1}{N_t^2} \left(\frac{1 - P_{\text{surv}|cc}}{P_{\text{surv}|cc}N_1} + \frac{1 - P_{\text{surv}|cc}^{(E)}}{P_{\text{surv}|cc}^{(E)}N_1^E}\right)} \quad (23)$$

Similar for the isotopic correction cross section with  $P_{\text{surv}|iso}$  the ratio of reconstructed  $^{12}C$  isotopes to all identified carbon isotopes in the x-position correlation plots for MWPC2 and MWPC3:

$$\Delta\sigma_{\text{stat.}|iso} = \sqrt{\left(\frac{\sigma_{iso}\Delta N_t}{N_t}\right)^2 + \frac{1}{N_t^2} \left(\frac{1 - P_{\text{surv}|iso}}{P_{\text{surv}|iso}N_1} + \frac{1 - P_{\text{surv}|iso}^{(E)}}{P_{\text{surv}|iso}^{(E)}N_1^E}\right)} \quad (24)$$

For viewing the statistical uncertainties of the total interaction cross section measuerments the uncertainties in the target thickness as well as the uncertainties of the carbon isotope surviving probability  $P_{\text{surv}|cc}$  and the  $^{12}C$  surviving probability  $P_{\text{surv}|iso}$  have to be accounted for:

$$\Delta\sigma_{\text{stat.}|tot} = \sqrt{\left(\frac{\sigma_{tot}\Delta N_t}{N_t}\right)^2 + \frac{1}{N_t^2} \left(\frac{1 - P_{\text{surv}|cc}}{P_{\text{surv}|cc}N_1} + \frac{1 - P_{\text{surv}|cc}^{(E)}}{P_{\text{surv}|cc}^{(E)}N_1^E}\right) + \frac{1}{N_t^2} \left(\frac{1 - P_{\text{surv}|iso}}{P_{\text{surv}|iso}N_1} + \frac{1 - P_{\text{surv}|iso}^{(E)}}{P_{\text{surv}|iso}^{(E)}N_1^E}\right)} \quad (25)$$

#### 4.6.2 Systematic Uncertainties

### 4.7 (Preliminary) Results Total Interaction Cross Section

### 4.8 Quasi-Free Scattering $^{12}C(p,2p)^{11}B$

this is a reference to C\*\*\*\*test \*\*\*bottomline: is this really just a subsection?\*\*\*\*\*

Notes:

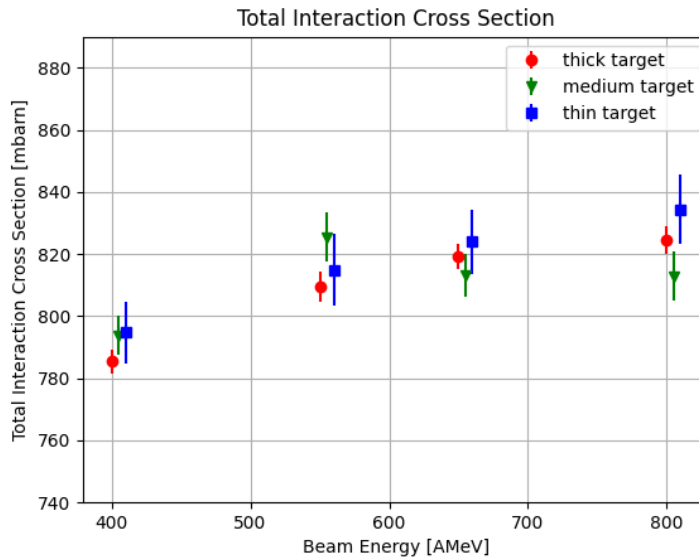


Figure 37: Total interaction cross section using the quadrant IV. selection in MWPC1 x-y plot (see figure 31) for the isotope correction and applying the geometric correction on the charge changing cross section.

- chapter introduction, first commissioning of p2p reactions at R3B,since first time CALIFA in Final frame and 35% filled in iPhos
- what do I have about calibration?
- channel identification -> Fragment Reconstruction
- Proton characteristics in Califa
- inner mom reconstruction, many features here to present
- Gamma Spectrum reconstruction / doppler correction (maybe I can use here my own clustering ML stuff?)
- appendum: separation energy reconstruction? aob?

## 4.9 reaction cross section Analysis

## 5 Results and Discussion

# Appendices

## A TWIN MUSIC Geometric Acceptance Correction via Efficiency Measurement

Instead of correcting the limited geometric acceptance of TWIN MUSIC via graphical fitting (see section 4.4) it is also feasible correcting via TWIN MUSIC efficiency measurement. The correction factor is given by:

$$\epsilon_{geo\_corr} = \frac{N_{MWPC1,MWPC2}}{N_{MWPC1,MWPC2,TWIN}} \quad (26)$$

where  $N_{MWPC1,MWPC2}$  corresponds to the number of events with a hit in MWPC1 and MWPC2 whereas  $N_{MWPC1,MWPC2,TWIN}$  imposes the further condition having a hit in TWIN MUSIC too.

The corresponding correction factor  $\epsilon_{geo\_corr}$  is consequently applied on all target and empty runs. The resulting corrected charge changing cross section is shown in figure 38. The same correction factor can be applied to the total interaction cross section as in figure 39.

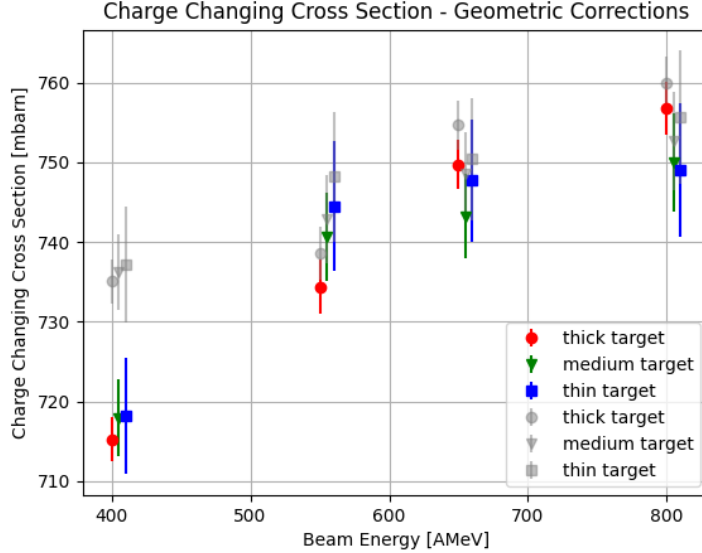


Figure 38: Charge changing cross section correction due to limited geometric acceptance of TWIN MUSIC via efficiency correction with MWPC1 and MWPC2. In gray: charge changing cross section measurements before applying corrections, as in figure 19

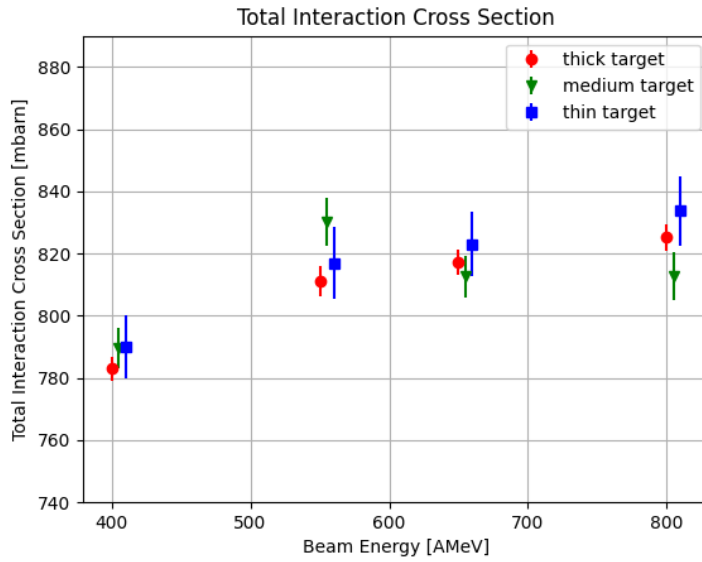


Figure 39: Total interaction cross section of  $^{12}\text{C} + ^{12}\text{C}$  using the TWIN MUSIC efficiency correction factor, see equation 26, to compensate for the limited geometric acceptance in TWIN MUSIC.

## B appendix-test

foo test appencdix of qfs

## C second stuff I want to add

hello here to add, end.

## References

- [1] O. Chamberlain and E. Segrè, “Proton-proton collisions within lithium nuclei,” *Physical Review*, vol. 87, no. 1, p. 81, 1952.
- [2] J. Cladis, W. Hess, and B. Moyer, “Nucleon momentum distributions in deuterium and carbon inferred from proton scattering,” *Physical Review*, vol. 87, no. 3, p. 425, 1952.
- [3] T. Maris, P. Hillman, and H. Tyrāln, “Quasi-elastic scattering and nuclear structure,” *Nuclear Physics*, vol. 7, pp. 1–9, 1958.
- [4] M. Patsyuk, J. Kahlbow, G. Laskaris, M. Duer, V. Lenivenko, E. Segarra, T. Atovullaev, G. Johansson, T. Aumann, A. Corsi, *et al.*, “Unperturbed inverse kinematics nucleon knockout measurements with a carbon beam,” *Nature physics*, vol. 17, no. 6, pp. 693–699, 2021.
- [5] G. Charpak, R. Bouclier, T. Bressani, J. Favier, and Č. Zupančič, “The use of multiwire proportional counters to select and localize charged particles,” *Nuclear Instruments and Methods*, vol. 62, no. 3, pp. 262–268, 1968.
- [6] J.-F. Martin, J. Taïeb, G. Boutoux, A. Chatillon, T. Gorbinet, E. Pellereau, L. Audouin, A. Heinz, H. Alvarez-Pol, Y. Ayyad, *et al.*, “Fission-fragment yields and prompt-neutron multiplicity for coulomb-induced fission of u 234, 235 and np 237, 238,” *Physical Review C*, vol. 104, no. 4, p. 044602, 2021.
- [7] GSI Helmholtzzentrum für Schwerionenforschung GmbH, “Large-acceptance dipole magnet glad.” [https://www.gsi.de/fileadmin/Kernreaktionen/GLAD\\_in\\_CaveC.jpg](https://www.gsi.de/fileadmin/Kernreaktionen/GLAD_in_CaveC.jpg), 2013. [Online; accessed September 09, 2024].
- [8] “Technical report for the design, construction and commissioning of the califa barrel.” [https://igfae.usc.es/~r3b/documentos/TDR/CALIFA\\_BARREL\\_TDR.pdf](https://igfae.usc.es/~r3b/documentos/TDR/CALIFA_BARREL_TDR.pdf). Accessed: 2024-09-24.
- [9] M. Bendel, *Entwicklung einer neuartigen Nachweismethode hochenergetischer Teilchen im CALIFA-Kalorimeter*. Dr., Technische Universität München, München, 2014. Technische Universität München, Diss., 2014.

- [10] “Technical report for the design, construction and commissioning of the califa endcap.” [https://edms.cern.ch/ui/file/1833748/2/TDR\\_R3B\\_CALIFA\\_ENDCAP\\_public.pdf](https://edms.cern.ch/ui/file/1833748/2/TDR_R3B_CALIFA_ENDCAP_public.pdf). Accessed: 2024-09-24.
- [11] J. Graña-González, J. Rodríguez-Sánchez, J. Benlliure, G. García-Jiménez, H. Alvarez-Pol, D. Cortina-Gil, L. Atar, L. Audouin, G. Authelet, A. Besteiro, *et al.*, “Fission studies in inverse kinematics with the r3b setup,” in *EPJ Web of Conferences*, vol. 290, p. 02015, EDP Sciences, 2023.
- [12] I. Holl, E. Lorenz, and G. Mageras, “A measurement of the light yield of common inorganic scintillators,” *IEEE Transactions on Nuclear Science*, vol. 35, no. 1, pp. 105–109, 1988.
- [13] A. Syntfeld-Kazuch, L. Swiderski, W. Czarnacki, M. Gierlik, W. Klamra, M. Moszynski, and P. Schotanus, “Non-proportionality and energy resolution of csi (tl),” *IEEE Transactions on Nuclear Science*, vol. 54, no. 5, pp. 1836–1841, 2007.
- [14] M. Winkel, *Implementierung und Erprobung einer digitalen Pulsformanalyse zur Auslese von Kalorimetern*. PhD thesis, Diplomarbeit, 2011.
- [15] M. O. Winkel, *Komplexe Pulsformalgorithmen und Teilchenidentifikation zur Echtzeit-Implementierung in CALIFA*. PhD thesis, Technische Universität München, 2016.
- [16] A.-L. Hartig, “Evolution of califa: From single detector modules to benchmark reactions,”
- [17] “Mesytec.” <https://www.mesytec.com/>. [Online; accessed September 29, 2024].
- [18] “Febex 3b-front end board with optical link extension.” <https://www.gsi.de/fileadmin/EE/Module/FEBEX/fbex3b.pdf>. [Online; accessed September 30, 2024].
- [19] K. Philipp, *Gamma detection with CALIFA*. PhD thesis, Technische Universität München, 2024.
- [20] GSI Helmholtzzentrum für Schwerionenforschung GmbH, “Exploder.” <https://www.gsi.de/en/work/forschung/experimentelektronik/digitalelektronik/digitalelektronik/module/lwl/exploder>. [Online; accessed September 30, 2024].

- [21] A. Bail, J. Taieb, A. Chatillon, G. Belier, B. Laurent, and E. Pellereau, “Time of flight measurement on the sofia experiment,” in *2011 2nd International Conference on Advancements in Nuclear Instrumentation, Measurement Methods and their Applications*, pp. 1–4, IEEE, 2011.
- [22] K. Boretzky, I. Gašparić, M. Heil, J. Mayer, A. Heinz, C. Caesar, D. Kresan, H. Simon, H. T. Törnqvist, D. Körper, *et al.*, “Neuland: The high-resolution neutron time-of-flight spectrometer for r3b at fair,” *Nuclear Instruments and Methods in Physics Research Section A: Accelerators, Spectrometers, Detectors and Associated Equipment*, vol. 1014, p. 165701, 2021.
- [23] K. Boretzky, G. Alkazov, L. Atar, T. Aumann, and C. Beinrucker, “Neuland—from double-planes to the demonstrator,” *GSI Sci. Rep.*, vol. 200, p. 2015, 2014.
- [24] L. Ponnath, *Precise Measurement of Nuclear Interaction Cross Sections with R3B*. PhD thesis, Technische Universität München, 2023.
- [25] “Mdpp-16 detector readout systems, mesytec.” <https://www.mesytec.com/products/nuclear-physics/MDPP-16.html>. [Online; accessed October 18, 2024].
- [26] K. Lau and J. Pyrlík, “Optimization of centroid-finding algorithms for cathode strip chambers,” *Nuclear Instruments and Methods in Physics Research Section A: Accelerators, Spectrometers, Detectors and Associated Equipment*, vol. 366, no. 2-3, pp. 298–309, 1995.